Coulomb breakup of ^{7}Li for nuclear astrophysics

Y. Tokimoto, H. Utsunomiya, T. Yamagata, and M. Ohta
Department of Physics, Konan University, 8-9-1 Okamoto, Higasinada, Kobe 658-8501, Japan

Y.-W. Lui and R. P. Schmitt
Cyclotron Institute, Texas A&M University, College Station, Texas 77843

S. Typel
Sektion Physik, Universität München, Am Coulombwall 1, D-85748 Garching, Germany

Y. Aoki
Institute of Physics, University of Tsukuba, Tsukuba, Ibaragi 305, Japan

K. Ieki
Department of Physics, Rikkyo University, Nishi-Ikebukuro, Tokyo 171, Japan

K. Katori
Institute of Physical and Chemical Research (RIKEN), Wako, Saitama 351-0198, Japan
(Received 13 September 2000; published 30 January 2001)

A new Coulomb breakup experiment was performed for ^{7}Li with an improved experimental technique and theoretical treatment. Energy spectra of α particles and tritons were examined to find the signature of post-Coulomb acceleration in the breakup of ^{7}Li at $E_{\alpha t}=0$. The data revealed the delayed nature of nonresonant breakup of astrophysical relevance that stems from quantum tunneling. Semiclassical discussions are presented of the lifetime of continuum states in ^{7}Li and distortion of relative kinetic energies between α and t by post-Coulomb acceleration. Dynamical calculations of Coulomb breakup were performed by solving a time-dependent Schrödinger equation. A simple potential model of ^{7}Li was employed. The dynamical calculations reasonably reproduced experimental cross sections for both resonant and nonresonant breakup with two key ingredients: higher order effects and mixture of $E1$ and $E2$ multipoles. Considering the dominant role of the first-order $E1$ nature in adiabatic Coulomb breakup, cross sections in the $v_\alpha \geqslant v_t$ branch at $7°-15°$ for ^{64}Zn and ^{90}Zr were used to deduce astrophysical S factors $S(E)$ for $t(\alpha,\gamma)^7$Li. They exhibit a moderate energy dependence at small energies. The strongly energy-dependent $S(E)$ resulted from the previous Coulomb breakup experiment based on cross sections with $v_\alpha \leqslant v_t$; they are most likely Coulomb distorted and are revised in the present work.

DOI: 10.1103/PhysRevC.63.035801 PACS number(s): 25.70.De, 21.10.Pc, 26.35.+c, 25.70.Mn

I. INTRODUCTION

The determination of cross sections for charged-particle reactions is of particular importance for astrophysics. Reaction rates serve as input to various astrophysical models such as primordial nucleosynthesis or stellar evolution. Ideally, cross sections are measured directly in experiments, however, in most cases a direct measurement is very difficult or even impossible at the relevant small energies since cross sections become very small because of Coulomb repulsion of the interacting particles. Often one has to rely on an extrapolation of the cross section to small energies. Alternative methods have been proposed where the considered reaction is not studied directly but a closely related process can be measured in the laboratory.

In the case of radiative capture reactions the Coulomb dissociation method has been used successfully as an indirect method in recent years. Here, the inverse reaction to radiative capture, i.e., the breakup of the nucleus produced in the fusion process, is studied during the scattering on a highly charged target, which supplies the necessary photons through its Coulomb field. The method was first proposed in detail in Ref. [1] and is reviewed in Refs. [2,3]. From the dissociation cross section the astrophysical S factor of the capture reaction can be extracted with the help of nuclear reaction theory. In order to obtain reliable information, the reaction mechanism has to be understood and the validity of the theoretical description has to be established.

The nuclide ^{7}Li is produced in the early universe via the $t(\alpha,\gamma)^7$Li reaction. The relevant energies are in the range of $0-500$ keV at $T_9=0.8$ [4]. Figure 1 summarizes available astrophysical S factors for the $t(\alpha,\gamma)^7$Li reaction. As of 1991, three direct measurements raised a question whether astrophysical S factors are energy dependent at small energies or not. The data of Griffiths *et al.* [5] showed constant S factors $[S(E)=0.064\pm0.016$ keV b] at energies down to 350 keV, while that of Schröder *et al.* [6] showed a marked rise to $S(0)=0.14\pm0.02$ keV b at small energies. The data of Burzyński [7] did not help to resolve the difference between the two data sets due to the limited energy range, i.e., $E\geqslant 297$ keV. A new direct measurement was undertaken by Brune, Kavanagh, and Rolfs [8], providing $S(E)$ in the

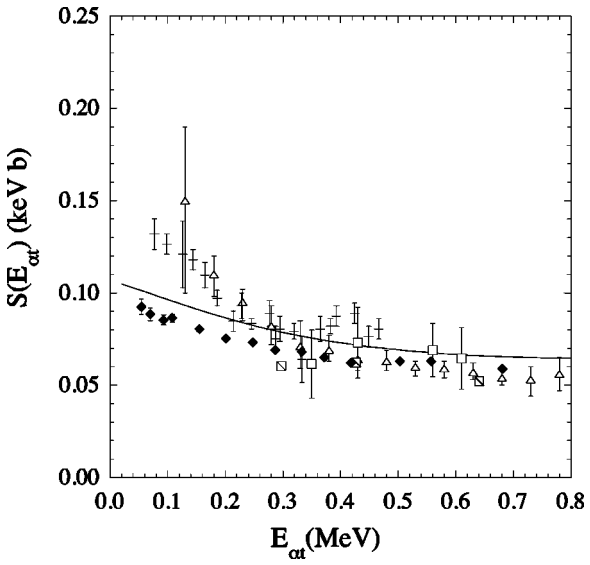

FIG. 1. Astrophysical S factors for $t(\alpha,\gamma)^7$Li. Results of direct measurements (squares by Griffiths *et al.* [5], slashed-squares by Burzyński *et al.* [7], crosses by Schröder *et al.* [6], filled diamonds by Brune *et al.* [8]) and the previous Coulomb breakup experiments (open triangles by Utsunomiya *et al.* [9]) are shown. The solid line stands for the result of our potential model calculation.

energy range 50–1200 keV with a systematic uncertainty of 6%. The data showed that $S(E)$ are indeed energy dependent, but more moderate toward $S(0)=0.1067(4)$ keV b than that of Schröder *et al.* [6]. There remains a significant discrepancy between the different sets of direct measurements and earlier experiments show large uncertainties. Thus, an independent determination of the low-energy S factor is worthwhile, but results from the previous Coulomb breakup experiment disagreed with direct measurements at small α-t relative energies.

A comparison of ^{7}Li [9] and ^{6}Li [10–12] Coulomb dissociation highlights some problems in determining the astrophysical S factor of the $t(\alpha,\gamma)^7$Li reaction. The radiative capture of α and deuteron is dominated by an $E2$ transition to the ^{6}Li ground state, which is the only bound state of the system. The $E1$ contribution is extremely small, becoming important only at very small α-d relative energies. At small projectile energies in Coulomb breakup of ^{6}Li, $E1$ transitions are strongly suppressed and can be neglected in the analysis. The fragments have nearly equal charge-to-mass ratios and effects from the postacceleration of α and deuteron in the target Coulomb field are not expected to change the relative momentum substantially. The radiative capture reaction $t(\alpha,\gamma)^7$Li can populate both the ground and first excited state of ^{7}Li. Since in Coulomb dissociation we only have an excitation from the ground state, information on capture to excited states has to be obtained from different sources, e.g., using branching ratios. The α-t radiative capture is dominated by $E1$ multipolarity with a small $E2$ contribution which is not known experimentally. In Coulomb excitation $E2$ transitions are enhanced as compared to $E1$ transitions. The angular distribution of the fragments can change through interference effects and additionally through post-Coulomb acceleration because of the different charge-to-mass ratio of α and triton. All these effects have to be considered if one tries to extract the S factor for the $t(\alpha,\gamma)^7$Li reaction from Coulomb breakup.

The importance of electromagnetic excitation in the breakup of ^{7}Li during the scattering on heavy targets was concluded from early experiments by Shotter *et al.* [13]. After that, Coulomb dissociation of ^{7}Li was extensively studied under various experimental conditions [9,14–17], however, a theoretical explanation of the data within the framework of first order perturbation theories was not satisfactory. Here, we report on new experimental results for both continuum and resonant breakup of ^{7}Li. They are compared to results from improved theoretical calculations of Coulomb dissociation which consider higher order effects as well as $E1$ and $E2$ multipoles.

The present work is organized as follows. In Sec. II we describe the experimental method used for the study of continuum and resonant breakup of ^{7}Li. In Sec. III the data reduction for determing the relative energy and cross section is presented. Effects of postacceleration of the fragments in the target Coulomb field are discussed for various observables in simple semiclassical models in Sec. IV. Section V defines the theoretical framework for the quantum-mechanical calculation of ^{7}Li breakup. In Sec. VI experimental results are compared to theoretical calculations. The astrophysical S factor of the $t(\alpha,\gamma)^7$Li reaction is determined in Sec. VII. Finally, we close with conclusions.

II. EXPERIMENTAL METHOD

A. Nonresonant breakup measurements

A beam of 42 MeV– ^{7}Li was provided by the 12 UD Pelletron tandem accelerator of University of Tsukuba. A variety of self-supporting foils were irradiated. Table I lists target nuclides and their areal densities. The beam current was collected by a micro Faraday cup with an electron suppressor mounted inside the scattering chamber. The beam intensity was 30–300 nA on target.

Figure 2 depicts the experimental setup. An Enge split pole magnetic spectrograph with $\rho_{\max}/\rho_{\min}\simeq 2.8$ and $\rho_{\max}=90$ cm (ESP90) was used to detect both α particles and tritons from breakup of ^{7}Li. An entrance aperture of the spectrograph was 20 mm wide, 10 mm high, at a distance of 270 mm from the target. Thus, pairs of the breakup fragments emitted into a solid angle of 2.74 msr were momentum-analyzed according to their magnetic rigidity and focused at different positions along the focal plane. A 37 cm (76 cm) focal plane detector consisting of a single resistive-wire proportional counter backed by a plastic scintillator was mounted on the low-momentum side (high-momentum side) to detect α particles (tritons). The anode was a Nichrome wire of 12.7 μm diameter. The pressure windows were 25.4 μm Kapton and the cathode foils were 25.4 μm aluminized Mylar. The proportional counter was operated with a P30 gas that flowed at 25 cm^3/min under 1 atm. The dead space between the two focal plane detectors was minimized to 10.5 cm. Photomultiplier tubes of 38 mm diameter (Hamamatsu R580) were mounted on low and high momen-

TABLE I. Experimental parameters for the nonresonant breakup experiment.

Target nuclide	Thickness (mg/cm^2)	Magnetic field (kG)	Detection angle (deg.)	Classical grazing angle (deg.)
^{27}Al	2.2	13.79	7, 10	15
^{58}Ni	4.8	13.79	10	27
^{64}Zn	3.9	13.79	7, 10, 12, 15, 17, 20	28
^{90}Zr	5.2	13.79	7, 10, 12, 15, 17, 20, 25, 30	36
^{120}Sn	6.4	13.79	25, 35	44
^{144}Sm	3.3	13.79	20, 25, 30, 35, 40	55
^{197}Au	10.3	13.79	30, 35, 40, 45, 50, 55, 60	73

tum ends of the short and long plastic scintillators, respectively. A thick magnetic shield especially on the low momentum side was essential so as not to reduce the light output from the photomultiplier tube due to a fringing field of the ESP90. Elastically scattered $^7Li^{3+}$ impinged on the dead space between the two detectors. Thus, the intense elastic scattering did not disturb the coincidence measurement.

The present detection of coincident α particles and tritons is called collinear detection, where the breakup fragments as well as their parent nucleus ^{7}Li, were emitted nearly at the same laboratory angle. Figure 3 shows the velocity diagram of the collinear detection. In the rest frame of the parent nucleus, there are two kinds of collinear configurations of $v_\alpha \geqslant v_t$ and $v_\alpha \leqslant v_t$, respectively. At the magnetic field of 13.79 kG, the detector arrangement covered the magnetic rigidity $B\rho \simeq 58.2$–76.9 kG cm for α particles and $B\rho \simeq 83.4$–119 kG cm for tritons. The magnetic rigidity covered kinetic energies 17–26 MeV for α particles and 12–21 MeV for tritons in the collinear breakup of ^{7}Li through continuum states at excitation energies from 2.47 MeV (the α-t threshold energy) to 2.97 MeV. In other words, α-t relative energies of 0–500 keV were covered. Measurements were made inside the classical grazing angles. Detection angles and the classical grazing angles are also listed in Table I.

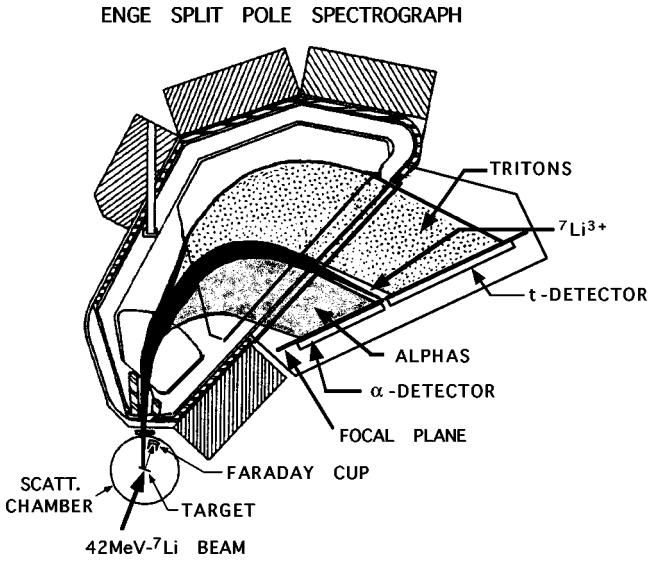

FIG. 2. Experimental setup for α-t coincidence measurements in nonresonant breakup of ^{7}Li at 42 MeV.

The medium plane of the ESP90 was found by maximizing the count rate for elastic scattering $^{12}C(\alpha,\alpha)$. The focal plane was found by achieving best energy resolution for the elastic scattering across the focal plane. The position (energy) resolutions of the short and long counters were 2.9 and 2.6 mm (218 and 173 keV) in FWHM, respectively. The energy calibration of the focal plane detectors was made with reactions of $^{12}C(\alpha,\alpha')^{12}C(0_1^+,2^+,0_2^+,3^-)$ for the α counter and $^{27}Al(\alpha,t)^{28}Si(0_1^+,2^+,4^+,0_2^+,3^-)$ for the triton counter at 29 MeV. A carbon foil of 99 μg/cm^2 and an aluminum foil of 58 μg/cm^2 were irradiated. An entrance collimator of the ESP90 used for the calibration was 0.343 msr.

Seven kinds of signals were processed into NORTHERN NS623 ADCs: four (H_α, L_α, H_t, L_t) from the high and the low momentum ends of the resistive wires of the two proportional counters, two (PL_α, PL_t) from the plastic scintillators and TAC started by the PL_α from the short (α) detector and stopped by the PL_t from the long (triton) detector. Energy loss information (ΔE) in the proportional counter were obtained by summing $H_{\alpha(t)}$ and $L_{\alpha(t)}$. Focal position spectra ($POS_{\alpha(t)}$) were software-generated into 1 k channels by $H_{\alpha(t)}/(H_{\alpha(t)}+L_{\alpha(t)})\times 1024$.

B. Resonant breakup measurements

We performed α-t coincidence measurements in breakup of ^{7}Li through the $7/2^-$ state at 4.63 MeV and the $5/2^-$ state

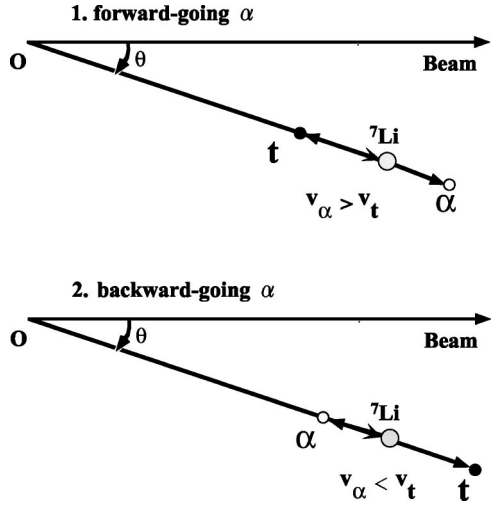

FIG. 3. Velocity diagram for the collinear projectile breakup.

TABLE II. Experimental parameters for the resonant breakup experiment.

Target nuclide	Thickness (mg/cm^2)	Magnetic field (kG)	Detection angle (deg.)
^{58}Ni	2.1	10.52 - 10.75	15, 20, 25, 30, 40
^{90}Zr	5.2	10.66, 10.60	20, 30
^{120}Sn	5.4	10.64, 10.58	30, 40
^{169}Tm	4.8	10.66, 10.61	40, 50
^{208}Pb	2.1	10.65	10

at 6.68 MeV. The measurement was limited to the collinear configuration of $v_\alpha \geqslant v_t$ because the momentum acceptance of the ESP90 ($\sim$280%) was not large enough to cover α-t pairs from the $5/2^-$ state in the other configuration. Kinetic energies expected in the resonant breakup were $E_\alpha \simeq 31$ MeV, $E_t \simeq 8.4$ MeV for the $7/2^-$ state with $\Gamma = 93 \pm 8$ keV and $E_\alpha \simeq 34 \pm 0.5$ MeV and $E_t \simeq 5.3 \pm 0.5$ MeV for the $5/2^-$ state with $\Gamma = 875^{+200}_{-100}$ keV [18].

For the resonant breakup experiment, the 37 and 76 cm focal-plane detectors were mounted on the high and the low momentum sides, respectively. Special attention was paid to the detection of the low energy tritons. We replaced the pressure windows and the cathode foils used for the nonresonant breakup experiment with thin Kapton (7.62 μm) and aluminized Mylar (7.62 μm), respectively. The proportional counter was operated with a P30 gas at 200 Torr. A movable blocker of 4 cm wide and 1 mm thick aluminum was used at forward angles to prevent elastically scattered $^7Li^{3+}$ from entering the short focal plane detector. Tritons at 10, 8, and 5 MeV that were produced using $^{27}Al(\alpha,t)^{28}Si(0^+,2^+,4^+)$ reactions at 19 MeV were successfully detected. The energy calibration of the focal plane detectors was made using (α,α') reactions on ^{12}C at 19 MeV at different settings of the magnetic field. Table II lists experimental parameters for resonant breakup.

III. DATA REDUCTION

A. Nonresonant breakup

1. Elastic breakup

Figures 4(a) and 4(b) show scatter plots of coincidence events in two planes: the light output from the plastic scintillator (PL) versus the focal plane position (POS) for the short and long detectors, respectively. Kinematical loci of α particles, deuterons, and tritons were clearly identified. Two types of coincidence events were observed, i.e., α-t and α-d coincidences.

Figure 5(a) shows an ungated TAC spectrum. Three peaks A, B, and C are seen in the spectrum. Peak A and majority of peak B correspond to α-d events resulting from one-neutron transfer reaction, i.e., (^{7}Li, ^{6}Li*) primarily leading to the 3^+ state in ^{6}Li at 2.185 MeV. The one-neutron transfer reaction was observed for all target nuclei. Peak C and minority of peak B correspond to α-t events. Figure 5(b) shows a TAC spectrum gated on the α-t coincidences. Peaks B and C correspond to coincidences with $v_\alpha \geqslant v_t$ and $v_\alpha \leqslant v_t$, respectively.

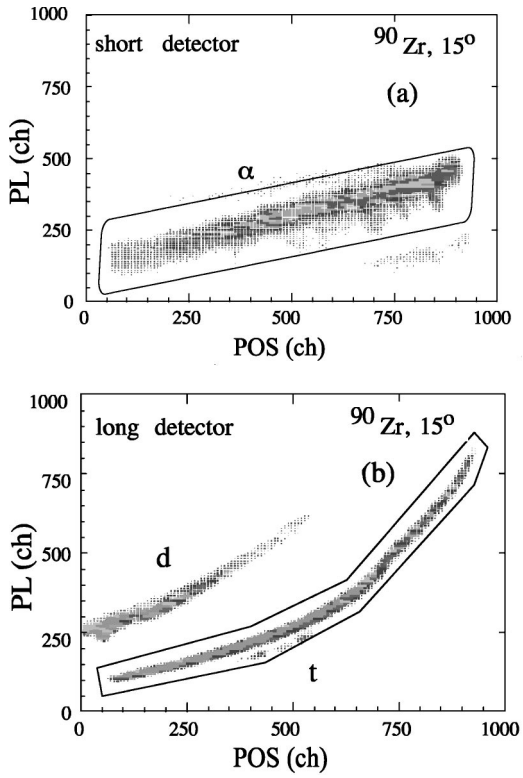

FIG. 4. Scatter plots of coincidence events in the focal-plane position (POS) versus the energy deposited in the plastic scintillator (PL) for the short detector (a) and for the long detector (b).

Sum energy spectra ($E_\alpha + E_t$) differentiated reaction Q values were produced to select elastic breakup in which a target nucleus remained in the ground state. A typical spectrum is shown in Fig. 6. The elastic breakup was unambiguously identified for such targets as ^{144}Sm, ^{120}Sn, ^{90}Zr, ^{64}Zn, ^{58}Ni, and ^{27}Al that have first excited states at a few MeV. For ^{197}Au and ^{169}Tm, however, the present energy resolution left some ambiguity for the excitation of low-lying states below 1 MeV.

A typical scatter plot of α-t coincidences in the POS_α versus POS_t plane is shown in Fig. 7. Kinematical loci for collinear elastic breakup with $v_\alpha \geqslant v_t$ and $v_\alpha \leqslant v_t$ are seen in the figure.

2. c.m. energy distribution

The focal positions (magnetic rigidity) for α particles and tritons were converted to laboratory kinetic energies. The laboratory energies were corrected for energy losses in the target foils, assuming that the breakup occurred at the midpoint of the target foil. The stopping power table of Northcliffe and Schilling [19] was used for this correction. Typical energy losses were $\sim$400 keV for α particles and $\sim$100 keV for tritons. The corrected energies were kinematically converted into energies with respect to the center of mass of the ^{7}Li+target system.

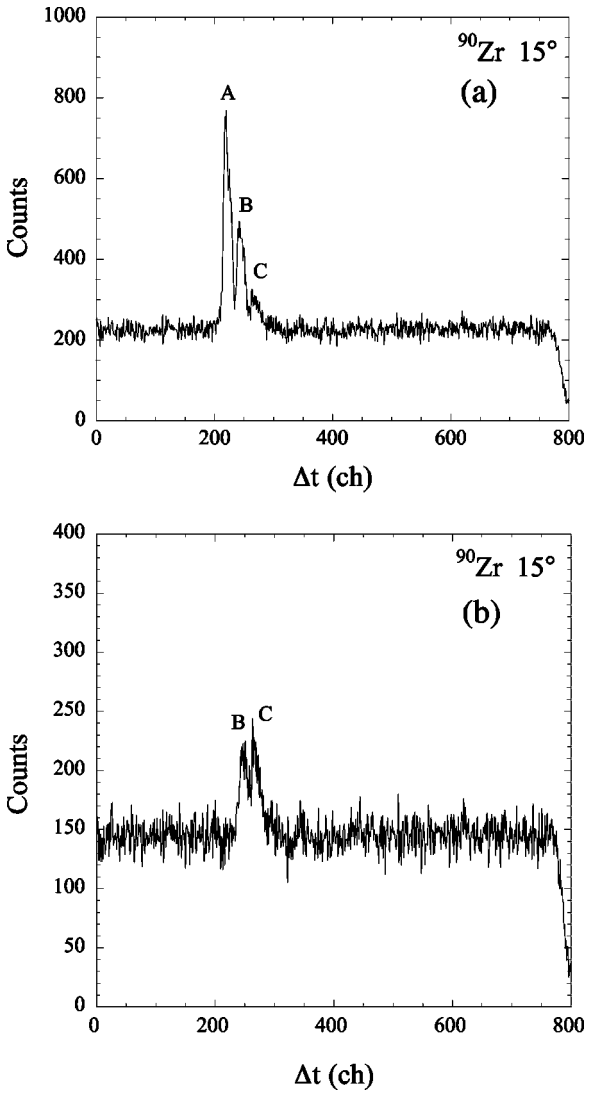

FIG. 5. TAC spectra: ungated (a) and gated on α-t coincidence events (b). Nonresonant breakup.

3. Relative energy distribution

Kinetic energies for a relative motion between α and t were computed from

$$E_{\alpha t}=\frac{1}{m_\alpha+m_t}(m_tK_\alpha+m_\alpha K_t-2\sqrt{m_tm_\alpha K_tK_\alpha}\cos\chi), \tag{1}$$

where m_i and K_i are, respectively, the mass and kinetic energy of particle $i(i=\alpha$ or $t)$, and χ is the angle between α and t emission axes. In this equation, K_i and χ can be either laboratory or c.m. quantities. The distribution of χ was calculated with a Monte Carlo method, resulting in a most probable value of 1.3° with a width of 2.3° in FWHM. The most probable value was used for χ. The energy resolution was estimated to be ~20 keV from error propagation based on Eq. (1) with $\Delta K_i/K_i=0.01$ and $\Delta\chi=2.3°$.

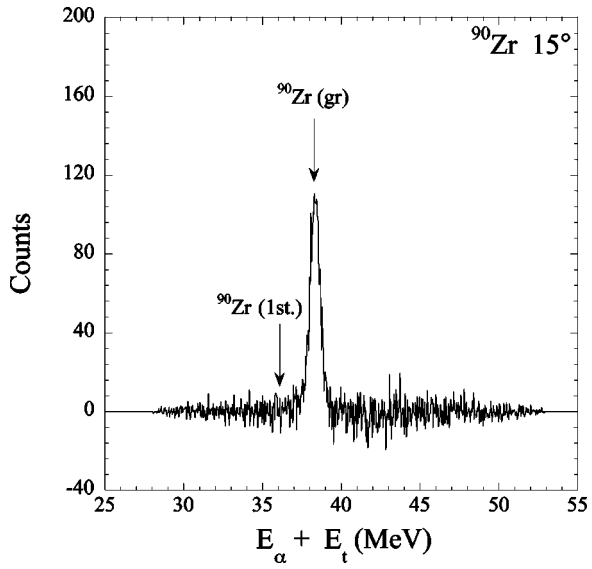

FIG. 6. Sum-energy spectrum ($E_\alpha+E_t$). Energies corresponding to elastic breakup and inelastic breakup leading to the first excited state in ^{90}Zr are indicated. Nonresonant breakup.

B. Resonant breakup

Figures 8(a) and 8(b) show scatter plots of coincidence events for the short detector in the *POS* versus *PL* plane and in the *POS* versus ΔE plane, respectively. α particles and deuterons formed the same kinematical loci in the *POS* versus *PL* plane, while they were well separated in the *POS* versus ΔE plane. Figure 7(c) shows a scatter plot in the *POS* versus *PL* plane for the long detector. Tritons were separated from α particles and deuterons in this plot. As in the nonresonant breakup experiment, abundant α-d coincidences were observed again.

Figure 9 shows a scatter plot in the *POS*1 versus *POS*2 plane with gates on α-t coincidences. α-t pairs from elastic breakup through the $7/2^-$ state at 4.63 MeV formed loci *A*. In contrast, we observed few events for the $5/2^-$ state at 6.68 MeV in the present experimental condition, forming loci *B*.

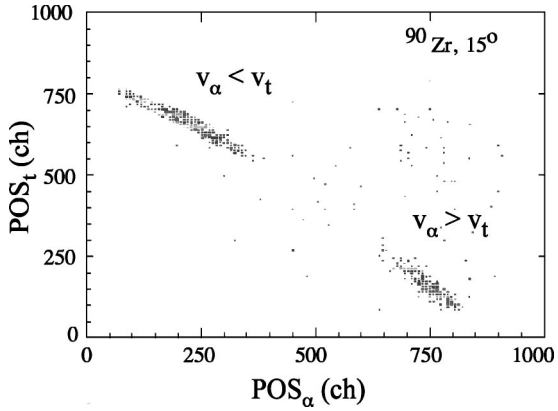

FIG. 7. Scatter plots of coincidence events in the focal-plane position for the long detector versus that for the short detector. Nonresonant breakup.

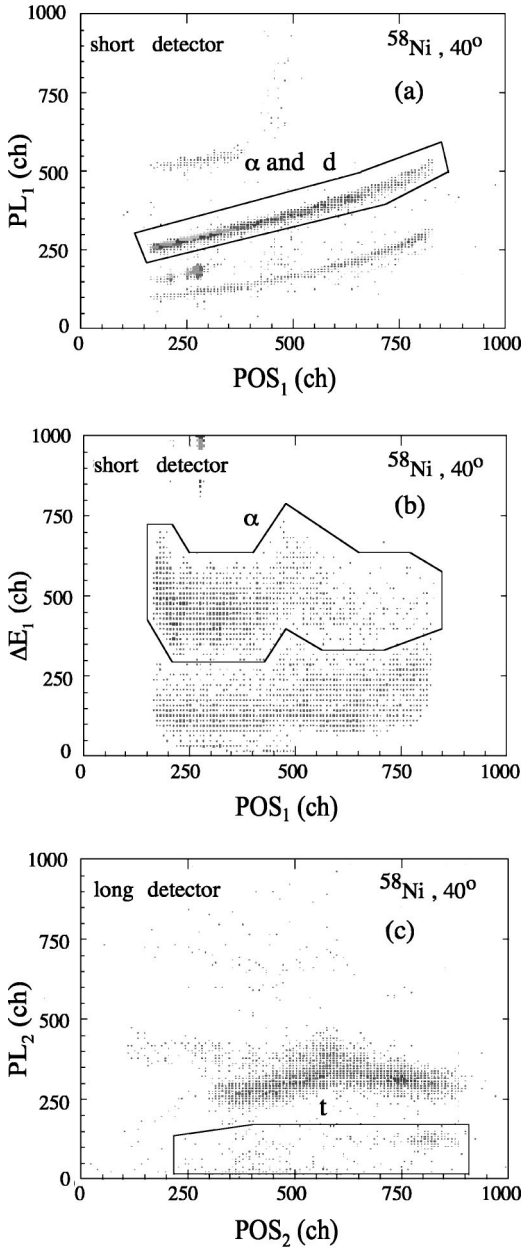

FIG. 8. Scatter plots of coincidence events in three planes: the focal-plane position (POS) versus the energy deposited in the plastic scintillator (PL) for the short detector (a), the focal-plane position (POS) versus the energy deposited in the proportional counter (ΔE) for the short detector (b), and the focal-plane position (POS) versus the energy deposited in the plastic scintillator (PL) for the long detector (c). Resonant breakup.

C. Breakup cross sections

Cross sections directly obtained from the coincidence measurements are triple differential cross sections in the laboratory system $d^3\sigma/dE_{\alpha(t)}d\Omega_{\alpha(t)}d\Omega_{t(\alpha)}$, where E_i is the kinetic energy and Ω_i is the solid angle for particle i. These cross sections were transformed into those in the rest frame of ^{7}Li, $d^3\sigma/dE_{\alpha t}d\Omega_{\mathrm{Li}}d\Omega_{\alpha t}$, where Ω_{Li} is the solid angle for the motion of the center of mass of the ^{7}Li system; $E_{\alpha t}$ and $\Omega_{\alpha t}$ are the kinetic energy and the solid angle for a relative motion between α and t, respectively. We discussed this transformation problem elsewhere [20] and performed the cross section transformation with two methods: one with Jacobians; and the other with a Monte Carlo method. The two methods have proven to give the same cross sections within statistical uncertainties.

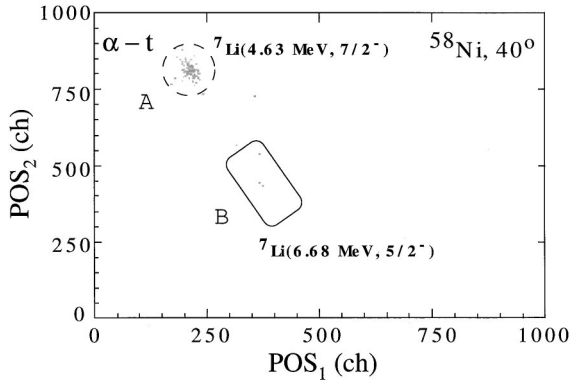

FIG. 9. Scatter plot of α-t coincidence events in the focal-plane position for the long detector ($POS1$) versus that for the short detector ($POS2$). Resonant breakup.

IV. SEMICLASSICAL CONSIDERATION OF POST-COULOMB ACCELERATION

A. Coulomb shift

Figure 10 shows c.m. energy distributions of α particles and tritons for ^{90}Zr at 15° and for ^{197}Au at 40°. While the distribution is symmetric for ^{90}Zr, it is highly asymmetric for ^{197}Au favoring forward-going α's and backward-going tritons. The coincidence yield is depleted at ~19 MeV (21 MeV) in the α spectrum and at ~14 MeV (15 MeV) in the t spectrum for ^{90}Zr (^{197}Au). The yield depletion ought to correspond to breakup at $E_{\alpha t}=0$ MeV.

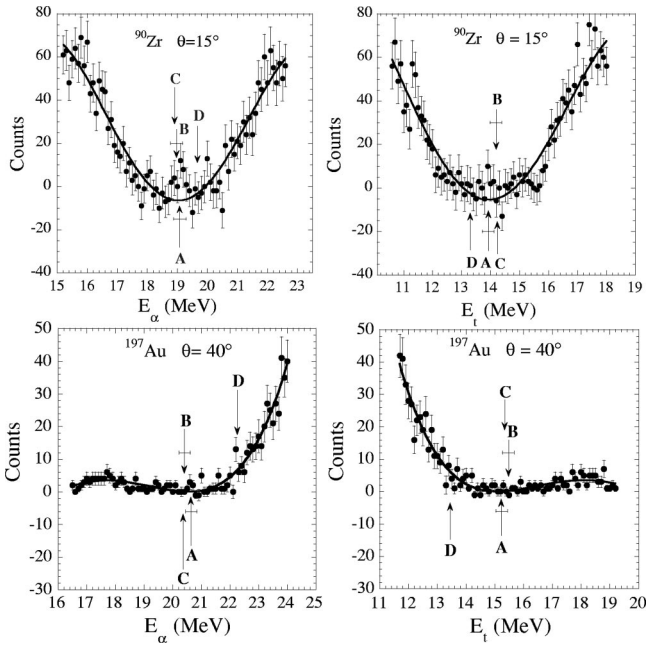

FIG. 10. c.m. energy distributions of α particles and tritons for ^{90}Zr and ^{197}Au. Nonresonant breakup.

We searched for the location of the yield depletion using two methods: (A) fits to the spectra with a fourth order polynomial function and (B) event-by-event analyses of energies leading to zero relative energy. The results of the two methods agree with each other within the estimated uncertainties (± 200 keV). In the figure, the results are indicated by arrows A and B.

Kinematics of breakup at $E_{\alpha t}=0$ in the c.m. system is simple as given in the Appendix. In a classical picture of the projectile breakup, energies of α and t fragments depends on the location of the ^{7}Li breakup: $E_\alpha(r)$ and $E_t(r)$. Using the distance r from the target, they are expressed by

$$E_\alpha(r)=E_\alpha(\infty)+\Delta_\alpha, \tag{2}$$

$$E_t(r)=E_t(\infty)+\Delta_t. \tag{3}$$

Here, $E_i(\infty)(i=\alpha$ or $t)$ is the c.m. energy for the aymptotic breakup [Eq. (A8)], i.e., breakup at the distance of infinity compared to the size of a nucleus, and Δ_i is a Coulomb shift with respect to the asymptotic breakup. It was assumed that after breakup at a distance r, the liberated α and t are under the influence of the target Coulomb field without interacting with each other.

The Δ_i is expressed in MeV by

$$\Delta_i=\frac{A_T}{A_a+A_T}\frac{Z_T Z_i^{\rm eff} e^2}{r}, \tag{4}$$

where A_i and Z_i are the mass number and the charge number ($i=\alpha$, t, a for projectile, T for target) and $Z_i^{\rm eff}$ is the effective charge number given by

$$Z_i^{\rm eff}=A_i\left(\frac{Z_i}{A_i}-\frac{Z_a}{A_a}\right). \tag{5}$$

In the limit of $A_T \gg A_a$, $\Delta_\alpha=-\Delta_t=2Z_T e^2/7r$ MeV. Note that α particles are *accelerated* and tritons are *decelerated* with respect to the asymptotic breakup in such a way that the acceleration and the deceleration fully compensate each other.

The arrow C represents the energy for asymptotic breakup $[E_i(\infty)]$ in which no postacceleration of breakup fragments in the target Coulomb field is expected. The energies for the breakup at the distance of closest approach in the Rutherford orbit are indicated by the arrows D. Figure 11 shows c.m. energy distribution for other targets. The difference in energy between the arrows C and D increases with the target charge number.

Figure 12 shows the location of the yield depletion for all targets and detection angles presently measured. The solid and open circles represent energies for α particles and tritons, respectively. The solid lines represent energies expected for asymptotic breakup, while the dashed lines for breakup at the distance of closest approach in the Rutherford trajectory. Clearly the nonresonant breakup is consistent with the asymptotic breakup.

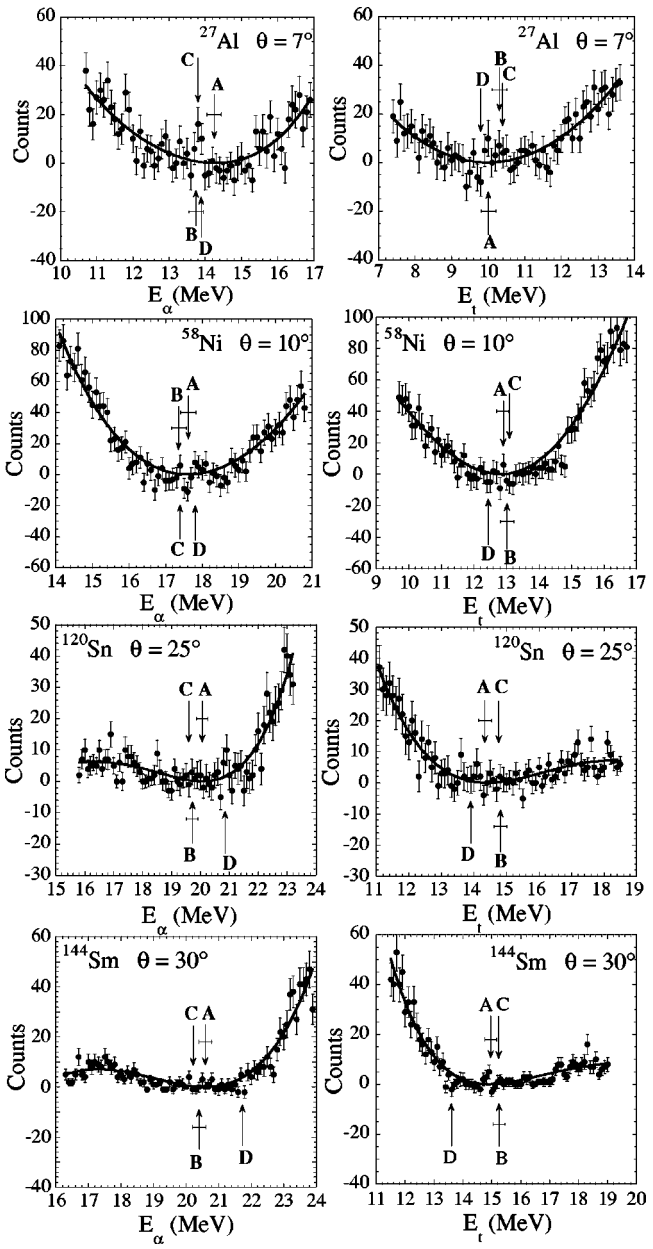

FIG. 11. c.m. energy distributions of α particles and tritons for ^{27}Al, ^{58}Ni, ^{64}Zn, ^{120}Sn, and ^{144}Sm. The yield depletion was located by the polynomial fit (arrow A) and the event-by-event analysis (arrow B). The location of the yield depletion expected for the asymptotic breakup and the breakup at the distance of closest approach in the Rutherford trajectory is shown by arrows C and D, respectively. Nonresonant breakup.

B. Quantum tunneling and lifetime of continuum states

It was tacitly believed that a ^{7}Li nucleus in continuum states above the α-t threshold behaves as kernels of Indian corn that burst to popcorn at the critical amount of heat. The term direct breakup well reflects this prompt nature with the threshold energy being the critical heat. However, the lack of post-Coulomb acceleration implies that the particle-unbound system may survive for a significant amount of time before decaying into an α particle and a triton. Although such system is no longer bound by a nuclear potential, it is bound by

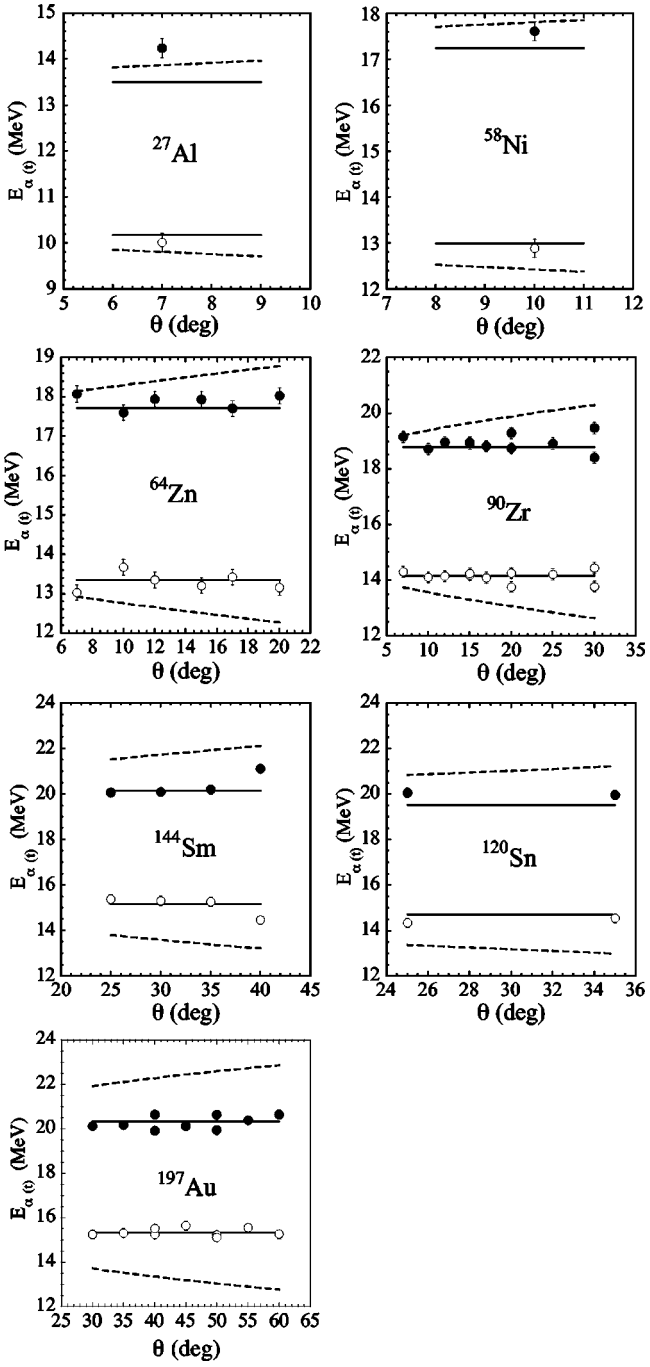

FIG. 12. Location of the yield depletion in comparison with those expected for the asymptotic breakup (solid lines) and for the breakup at the distance of closest approach in the Rutherford trajectory (dashed lines). Nonresonant breakup.

a Coulomb barrier between α and t. One may remember that nonresonant thermonuclear reactions between two charged particles in stars take place over the Gamow peak by tunneling through a Coulomb barrier [21,22]. It is this continuum state that is populated after tunneling through the Coulomb barrier.

Figure 13 schematically shows the nuclear and Coulomb potentials between α and t as a function of the distance r. The height of the Coulomb potential is 0.48 MeV at r $=6.0$ fm. By definition $V(r)=0$ at the α-t threshold. Assuming that a continuum state in ^{7}Li immediately above the threshold is a cluster state consisting of an α particle and a triton, it is possible to evaluate the tunneling lifetime of the state. In an analogy to the α decay theory [23], the particle decay rate (λ) of the unbound system can be defined by

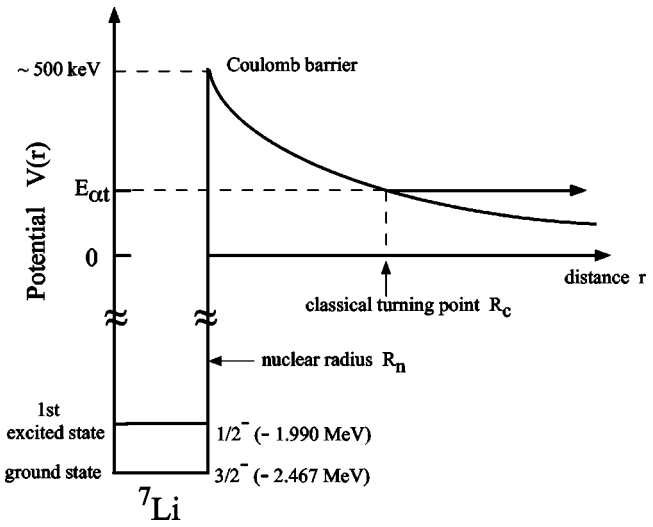

FIG. 13. Nuclear and Coulomb potentials between α and t as a function of distance r.

$$\lambda_l = \omega_l P_l , \tag{6}$$

where ω_l is the number of particles with relative angular momentum l that appear at the nuclear surface per second and P_l is the transmission probability of the potential barrier. For simplicity, we treat the case $l=0$ because radiative capture at small energies is dominated by s waves.

The frequency of s-wave vibration can be estimated by $v/2R$ with the velocity of α-t relative motion v and the nuclear radius R [23]. For a resonant state, one may express ω_0 by $\omega_0=(3v/R)\theta_0^2$ [21]. Here θ_0^2 is the dimensionless reduced width, representing a measure of to what degree the relevant state can be described as a cluster state of α and t. The simple estimate of the s-wave frequency corresponds to $\theta_0^2=1/6$.

We evaluated the transmission probability in the Wentzel-Kramers-Brillouin (WKB) approximation as [21]

$$P_0 \approx \left(\frac{B}{E_{\alpha t}}\right)^{1/2} \exp\left\{-4\eta\left[\frac{\pi}{2} - \arcsin\left(\frac{E_{\alpha t}}{B}\right)^{1/2} - \left(\frac{E_{\alpha t}}{B}\right)^{1/2}\left(1-\frac{E_{\alpha t}}{B}\right)^{1/2}\right]\right\}, \tag{7}$$

where $\eta = Z_t Z_\alpha e^2/\hbar v$ is the Sommerfeld parameter and $B = Z_t Z_\alpha e^2/R$ is the height of the Coulomb potential. At $E_{\alpha t} \ll B$ the exponent approaches $-2\pi\eta$ and we obtain the Gamow factor $\exp(-2\pi\eta)$ for s-wave capture. The WKB solution for the transmission probability differs from the Gamow factor by an additional factor $(B/E_{\alpha t})^{1/2}$.

Figure 14 shows the lifetime ($\tau=1/\lambda$: reciprocal of the decay rate) of the continuum states estimated with R of 4.75

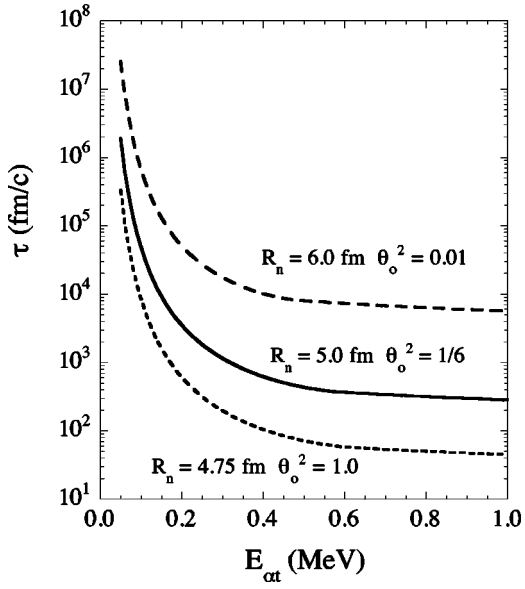

FIG. 14. Lifetimes of continuum states as a function of excitation energy from the α-t threshold at 2.47 MeV.

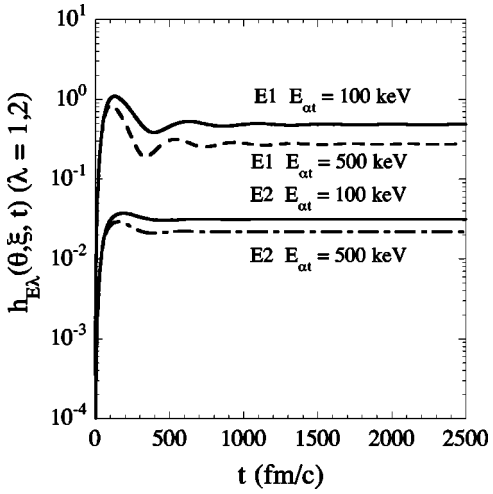

FIG. 15. Time-dependence of the quantity $h_{E\lambda}$ defined by Eq. (10).

– 6.0 fm and θ_0^2 of 0.1–1.0. The variation of R well characterizes the thickness of the potential barrier in view of the fact that the microscopic intercluster nuclear plus Coulomb potential by Kajino [24] crosses zero at 4.75 fm and reaches a barrier top at 6.0 fm.

It is noted that the lifetime can readily exceed the nuclear transit time of the order of 100 fm/c which can be evaluated from $\tau_n \approx (R_a + R_T)/V$ with velocity at the distance of closest approach (V) and radii of the projectile and target (R_a, R_T). It can be even larger than those of resonance states in ^{7}Li: $\tau = 225$ fm/c($\Gamma = 875$ keV) for the $5/2^-$ state at 6.68 MeV and $\tau = 2122$ fm/c($\Gamma = 93$ keV) for the $7/2^-$ resonant state at 4.63 MeV. The lifetime against particle decay naturally becomes very large at small energies. The particle decay may give way to gamma decay in the extreme.

It may be instructive to roughly estimate the time needed for the two fragments to make a full separation without tunneling through a Coulomb potential. Traveling r [fm] for a full separation, it takes $894 r/E_{\alpha t}^{1/2}$ [fm/c] at an energy $E_{\alpha t}$ [keV]. It takes 1287 fm/c to travel to the classical turning point ($r = 14.4$ fm) at $E_{\alpha t} = 100$ keV. One can see that the traveling time is significantly prolonged by the quantum tunneling.

C. Relative energy distribution

Projectile breakup into two charged fragments through continuum states immediately above a particle threshold is not prompt breakup but delayed breakup. This delayed nature stems from quantum tunneling through a Coulomb barrier between two charged constituents. As a result, postacceleration of the breakup fragments in the target Coulomb field is strongly suppressed. This feature may help to resolve or at least to ease a potential problem known as post-Coulomb acceleration in the Coulomb dissociation method [25].

Let us evaluate the Coulomb distortion of the α-t relative energy caused by the post-Coulomb acceleration. For simplicity, we assume that the Coulomb excitation takes place at the distance of closest approach.

To investigate to what extent this assumption is justified, we consulted to the first-order perturbation theory of Coulomb excitation [26].

The differential cross section is written as

$$\frac{d\sigma_{E\lambda}}{d\Omega} = \left(\frac{Z_T e}{\hbar v}\right)^2 a^{-2\lambda+2} B(E\lambda) \frac{df_{E\lambda}}{d\Omega}, \tag{8}$$

where v is the velocity, a is half the distance of closest approach in a head-on collision, and $B(E\lambda)$ is the reduced transition probability with multipole order $E\lambda$. The function $df_{E\lambda}/d\Omega$ for orbital integrals can be written as

$$\frac{df_{E\lambda}}{d\Omega} = \lim_{\tau\to\infty} h_{E\lambda}(\theta, \omega, \tau) \tag{9}$$

with

$$h_{E\lambda}(\theta, \omega, \tau) = \frac{4\pi^2 a^{2\lambda} v^2}{(2\lambda+1)^3} \sin^{-4}\frac{\theta}{2} \sum_{\mu} \left| Y_{\lambda\mu}\left(\frac{\pi}{2}, 0\right)\right|^2 \times \left| \int_{-\tau}^{+\tau} \frac{(x+iy)^{\mu}}{r^{\lambda+\mu+1}} e^{i\omega t} dt \right|^2. \tag{10}$$

The (x,y) are Cartesian coordinates and r is the radial coordinate of the projectile in the focal system of the hyperbolic orbit [26], ω is the nuclear frequency for Coulomb excitation and θ is the scattering angle. The $Y_{\lambda\mu}(\pi/2,0)$ are the spherical harmonics. Note that the function $h_{E\lambda}$ can be evaluated over the time interval from $-\tau$ to τ around time zero defined at the classical turning point.

Figure 15 shows a typical time dependence of $h_{E\lambda}$. The time interval for Coulomb excitation essentially concentrates over ± 500 fm/c around $t = 0$, independent of the multipolarity $E1$ and $E2$.

The *nuclear clock* of measuring the lifetime of continuum states now starts at the time of Coulomb excitation of

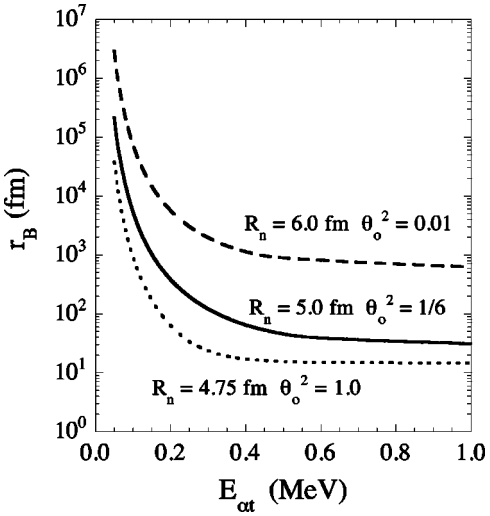

FIG. 16. Distance between projectile and target at which nonresonant breakup takes place. See text for details.

^{7}Li($t=0$). In the focal system, the distance between projectile and target (r) is expressed by

$$r = a(\varepsilon \cosh s + 1), \tag{11}$$

where the eccentricity parameter (ε) is related to the scattering angle (θ) by $\varepsilon = 1/\sin(\theta/2)$. The parameter s is related to time t by

$$t = \frac{a}{v}(\varepsilon \sinh s + s). \tag{12}$$

By putting the meanlife of the continuum states (τ) into t, one can obtain the location where breakup takes place. The location of breakup (r_B) thus determined for ^{197}Au is shown in Fig. 16. The Coulomb energy which the particle i($i=\alpha$ or t) gains after breakup is expressed by

$$E_i - E_i^l = \frac{A_T}{A_a + A_T}\frac{Z_i Z_T e^2}{r_B}, \tag{13}$$

where A is the mass number, the final kinetic energy E_i corresponds to the experimental observable, and E_i^l is the local kinetic energy at the breakup point.

The Coulomb shift $\Delta E = E_i - E_i^l$, for $\theta_0^2 = 1/6$ is shown in Fig. 17. For the collinear branch of $v_\alpha \geqslant v_t$ ($v_\alpha \leqslant v_t$), the shift amounts to 0.47 (−0.80) keV at $E_{\alpha t} = 100$ keV, 7.9 (−17) keV at 200 keV, and 26 (−67) keV at 300 keV.

The relative energy was calculated by putting either the asymptotic energy (E_i) or the local energy at the breakup point (E_i^l) into K_i of Eq. (1). The results for E_i and E_i^l are shown by the solid and open circles, respectively, in Fig. 18 for the ^{90}Zr data.

The cross sections in the collinear branch of $v_\alpha \geqslant v_t$ are not much affected by the post-Coulomb acceleration, whereas those in the branch of $v_\alpha \leqslant v_t$ are seriously distorted. Thus, the post-Coulomb acceleration effect is literally vanishing in the branch of $v_\alpha \geqslant v_t$, whereas it is surviving in the branch of $v_\alpha \leqslant v_t$.

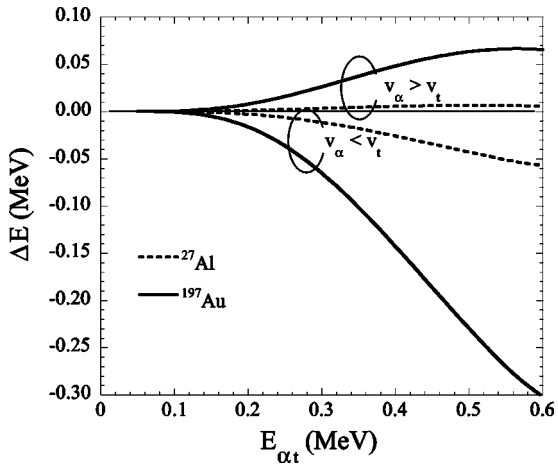

FIG. 17. Coulomb postacceleration [$\Delta E = E_i - E_i^l$ in Eq. (13)] of breakup fragments in the Coulomb field of target nuclei.

V. QUANTUM-MECHANICAL TREATMENT OF POST-COULOMB ACCELERATION

The traditional approach for the theoretical description of Coulomb excitation and breakup is the semiclassical approximation [26], i.e., the projectile moves on a classical trajectory in the Coulomb field of the target and the excitation of the projectile is treated quantally. In principle, the full system of projectile and target should be treated quantum-mechanically as it is done in a number of approaches using different approximations depending on the system under investigation [27,28]. However, an exact quantum-mechanical solution of the problem is beyond the current computational capabilities. Under most experimental conditions the semiclassical approach is valid since the Sommerfeld parameter

$$\eta = \frac{Z_a Z_T e^2}{\hbar v} \tag{14}$$

with charge numbers Z_a and Z_T of projectile and target and relative velocity v is much larger than 1.

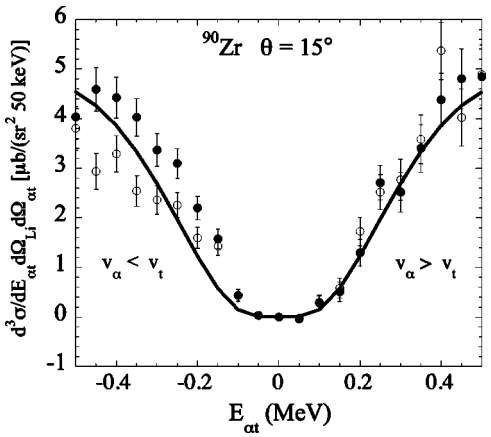

FIG. 18. Relative energy distributions obtained by putting asymptotic energies of experimental observables (solid circles) or local energies, E_i^l in Eq. (13), (open circles) into Eq. (1).

TABLE III. Depths of the Woods-Saxon potential for various partial waves c in the ^{7}Li potential model.

J_c	1/2	3/2	1/2	5/2	3/2	7/2	5/2
l_c	0	1	1	2	2	3	3
V_c [MeV]	62.74	75.031	73.392	64.41	60.42	72.08	64.25

Usually one relies on first order perturbation theory in order to calculate the excitation probability, thus neglecting the dynamic evolution of the projectile system. This corresponds to one-photon exchange between target and projectile and gives rise to the introduction of equivalent (or virtual) photon numbers depending on the multipolarity of the exchanged photon. The perturbative approach has the advantage of being independent of the nuclear model of the system. In the case of excitations of the projectile to bound states higher order effects are conveniently included by extending the perturbative approach to second order contributions to the excitation amplitude [26] or by coupled-channels calculations considering all bound intermediate states. For a breakup into continuum states an extension of the first order perturbation theory to second and third order contributions was developed in Refs. [29–31] which can be applied for high projectile energies. Other approaches to include higher order effects are coupled-channels calculations [32,33], where the continuum has to be discretized in order to avoid divergences in the transition matrix elements.

The most general nonperturbative method for the description of Coulomb (+ nuclear) breakup in the semiclassical approximation is the solution of the time-dependent Schrödinger equation. The time evolution of the projectile system is treated dynamically and the Coulomb (nuclear) potential of the target acts as a time-dependent perturbation. This framework has been used in order to study higher order effects in the Coulomb dissociation of nuclei such as ^{8}B, ^{11}Li, and ^{11}Be [34–39]. Here it will be used for the breakup of ^{7}Li. The numerical methods and technical details for the solution of the time-dependent Schrödinger equation are given in Ref. [40] and only a few comments about the physics input and theoretical improvements will be sufficient here.

A. The nuclear model for ^{7}Li

In our calculation we use a potential model for the ^{7}Li nucleus. We assume that it consists of α and t clusters which remain unaffected during the excitation process. The wave functions for the α-t relative motion are obtained by solving the stationary Schrödinger equation with central potentials of Woods-Saxon shape

$$V_c(r) = \frac{-V_c}{1+\exp[(r-R)/a]} \tag{15}$$

with radius $R=2.39$ fm and diffuseness parameter $a=0.68$ fm. The depths V_c of the potential are adjusted in each partial wave $c=(J_c,l_c)$ in order to give the experimental energies of the bound states and resonances or the scattering phase shifts. The values for V_c are given in Table III.

TABLE IV. Properties of the ^{7}Li system in the potential model in comparison to experimental data [18,8].

	Theory	Experiment
Width Γ/keV of $\frac{7}{2}^-$ resonance	88.3	93 ± 8
Width Γ/keV of $\frac{5}{2}^-$ resonance	862	875^{+200}_{-100}
Electric quadrupole moment of ground state Q_e/mb	-43.1	-40.6 ± 0.8
$B(E2,\frac{3}{2}^-\rightarrow\frac{1}{2}^-)/e^2$ fm^4	6.15	8.3 ± 0.5
Astrophysical S factor $S(0)$/keV b	0.1068	0.1067 ± 0.0068
Branching ratio $R(\mathrm{DC}\rightarrow\frac{1}{2}^-/\mathrm{DC}\rightarrow\frac{3}{2}^-)$	0.429	0.453 ± 0.020 0.437 ± 0.022

The total angular momentum J_c is obtained by coupling the orbital angular momentum l_c with the spin $s=\frac{1}{2}$ of triton. In our model we only consider s, p, d, and f waves, resulting in 32 channels from all possible values of J_c and its projection M_c.

In Table IV we compare properties of the ^{7}Li nucleus in our model with experimental data. The astrophysical S factor of our model calculation is shown in Fig. 1 in comparison with the results of the various direct measurements. We find good agreement with the experimental data. From these results we conclude that our model describes the ^{7}Li system sufficiently well.

B. Solving the time-dependent Schrödinger equation

We assume that the center of mass of the ^{7}Li system moves on a hyberbolic trajectory in the target Coulomb field during the scattering, see formulas (11) and (12). The orbit is determined by the initial velocity and the scattering angle. The projectile experiences a time-dependent Coulomb plus nuclear perturbation

$$V(\vec{r},t) = V_C(\vec{r},t) + V_N(\vec{r},t), \tag{16}$$

where $\vec{r}=\vec{r}_\alpha-\vec{r}_t$ is the relative vector between the two clusters. The Coulomb contribution to the perturbation is given by

$$V_C(\vec{r},t) = V_C^{\alpha T}(|\vec{r}_\alpha-\vec{R}(t)|) + V_C^{tT}(|\vec{r}_t-\vec{R}(t)|) - V_C^{\mathrm{Li}\,T}(|\vec{R}(t)|) \tag{17}$$

with the Coulomb potential

$$V_C^{cT}(R) = Z_c Z_T e^2 \begin{cases} \dfrac{1}{2R_T}\left(3-\dfrac{R^2}{R_T^2}\right) & \text{for} \quad R\leqslant R_T, \\ \dfrac{1}{R} & \text{for} \quad R>R_T \end{cases} \tag{18}$$

between nucleus c and the target T. We assume a homogeneous charged sphere for the target charge distribution with radius $R_T=1.3A_T^{1/3}$ [fm] at position $\vec{R}(t)$. The Coulomb interaction $V_C^{\mathrm{Li}\,T}$ between ^{7}Li and the target is subtracted since

it is responsible for the Coulomb scattering of the c.m. which is already included in the description. The nuclear contribution to the breakup will be neglected in the following, since we are interested in higher order effects caused by the long-range Coulomb interaction. The scattering angle of the ^{7}Li system in the experiment was chosen to be smaller than the classical grazing angle (see Table I). Therefore we expect only small contributions from nuclear breakup, but see also the discussion of the comparison between experimental and theoretical cross section.

The time-dependent wave function of the system is expanded into partial waves with all possible values of J_c and M_c. The radial channel wave functions are discretized on a mesh with exponential increase of the step size. Starting with 0.3 fm at $r=0$ fm we cover a range of 900 fm with 400 mesh points. The perturbation potential (16) is expanded into multipoles where we take into account only multipolarities up to $\lambda=2$. We obtain a time-dependent coupling of the different partial waves which causes the transitions during the scattering. Usually the Coulomb potential of a pointlike target is used where the multipole expansion can be done analytically. We perform a numerical expansion of the more realistic Coulomb potential (18) in the full calculation.

The time integration is started with the normalized wave function of the ^{7}Li ground state at a distance $r_{\rm int}$ which corresponds to 15 times the minimal distance between the projectile and the target. This value has been chosen since we are in the adiabatic regime of Coulomb excitation and the perturbation potential decreases at least with r^{-2}, thus at this distance it has a strength less than 0.5% of its maximum value. The time-evolution is followed in time steps of approximately 1 fm/c until the distance $r_{\rm int}$ is reached again where the perturbation potential can be neglected. The final wave function is a linear combination of the ground state and all bound and scattering states of the α-t system in our model. Care has been taken that unphysical bound states in our model are not populated during the excitation process. Since we have a fourfold degeneracy of the ground state of total angular momentum $\frac{3}{2}$ four independent calculations have to be performed for every combination of target and scattering angle.

Figure 19 shows the time evolution of the radial probability $\ln P_{\rm cont}(r,t)$ of finding the projectile system in continuum states for ^{197}Au at 50°. Here $P_{\rm cont}(r,t)=\int d\Omega_r|\Psi_{\rm cont}(\vec{r},t)|^2$ with the continuum wave function $\Psi_{\rm cont}(\vec{r},t)$. The continuum wave function was obtained by projecting the bound state contributions out of the full time-dependent wave function $\Psi(\vec{r},t)$. $t=0$ is defined at the distance of closest approach. Before $t=0$, the Coulomb excitation leads to an increase of the probability for small values of r corresponding to the spatial extension of the initial wave function. After the maximum of the probability is reached around $t=0$, a wave packet starts to propagate outwards. At the same time, a large fraction of the probability remains in the nuclear interior. This corresponds essentially to the excitation of the $7/2^-$ resonance which has a lifetime of approximately 2.1×10^3 fm/c.

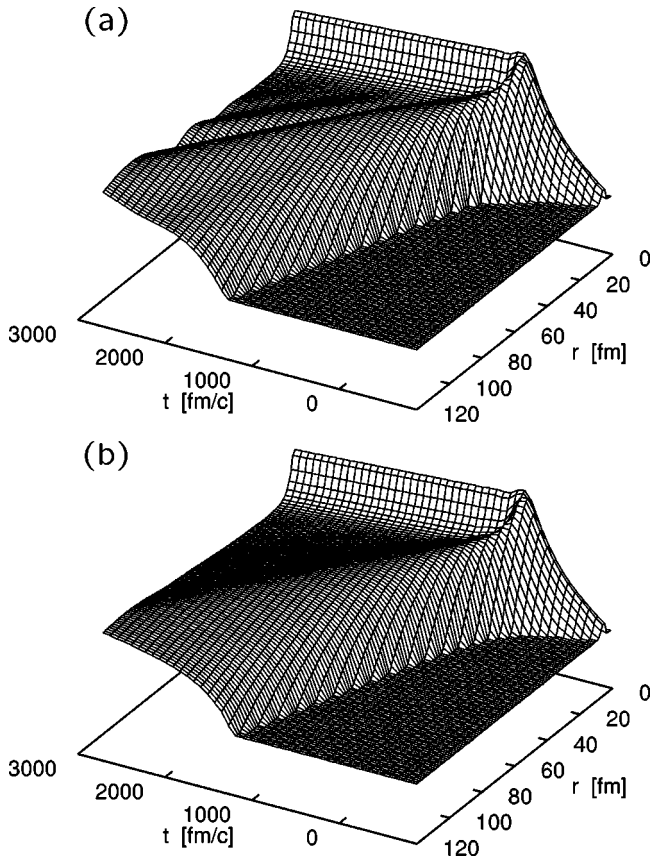

FIG. 19. Time dependence of the probability $\ln P_{\rm cont}(r,t)$ of finding the α and t fragments at a distance r in a scattering state (see text). (a) first order calculation, (b) dynamical calculation for a ^{197}Au target, a projectile energy of 42 MeV, and a ^{7}Li scattering angle of 50°.

Figure 20 shows the time-evolution of the triton angular distribution $\ln P_{\rm cont}(r_t,\varphi_t,t)$ in the rest frame of ^{7}Li within the scattering plane. A coordinate system was employed such that the projectile is at rest; it is oriented in a way where the z axis is perpendicular to the scattering plane and the trajectory of the target is symmetric to the x axis. r_t is the distance of the triton from the center of mass of ^{7}Li and φ_t is the azimuthal angle. The central peak corresponds to the $7/2^-$ state. The time evolution of its excitation, survival, and decay is clearly seen. In the first order calculation, the triton is emitted preferably in the direction antiparallel to the target. In contrast, the dynamical calculation shows a different distribution of the triton emission.

C. Calculation of cross sections

From the time-evolved wave function we obtain the amplitude a_{fi} for the excitation of the ^{7}Li ground state i to a final state f by projecting onto the corresponding wave function which is a solution of the stationary Schrödinger equation of the ^{7}Li system. This can be either a bound state or a continuum state with relative momentum $\vec{p}_{\alpha t}$. The transition amplitude $a_{fi}(\vec{p}_{\alpha t})$ contains the information about the direction of the emitted fragments and enters into the expression for the triple differential cross section

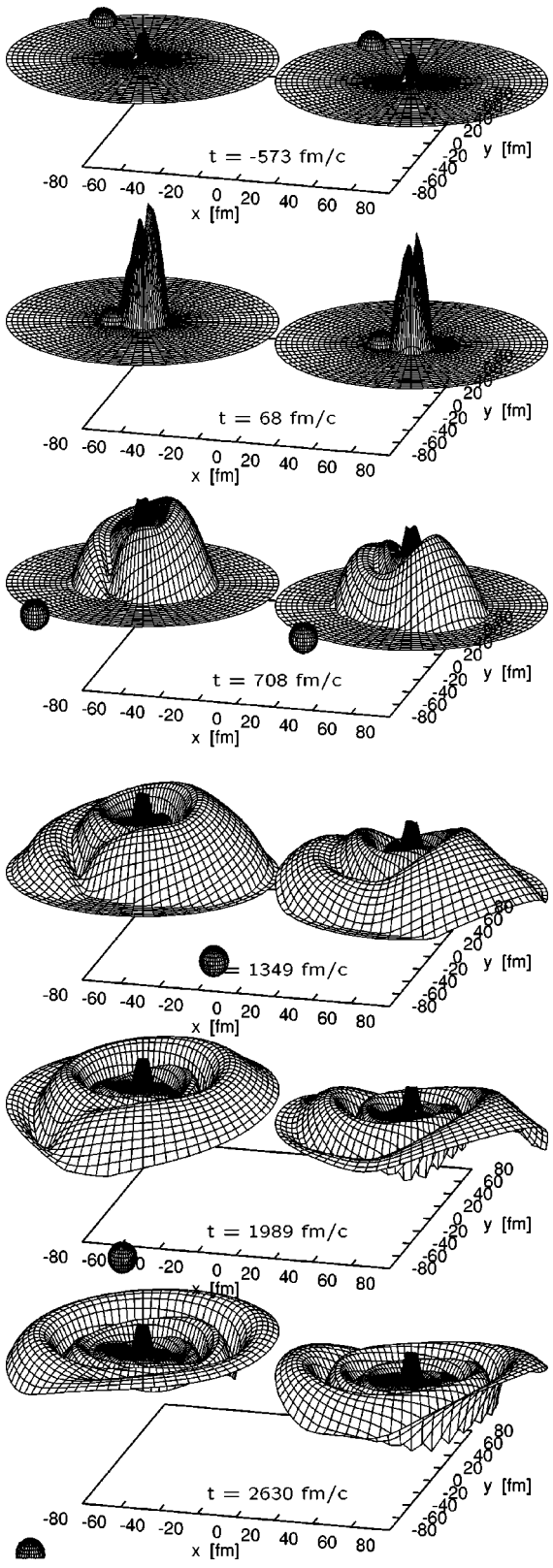

FIG. 20. Probability $\ln P_{\rm cont}(r_t,\varphi_t,t)$ of finding the triton at a distance r_t and an azimuthal angle φ_t in the scattering plane for different time-steps in the evolution of the breakup reaction. Left: first order calculation, right: dynamical calculation for the same conditions as in Fig. 19. The position and size of the target in the scattering plane is indicated by a sphere.

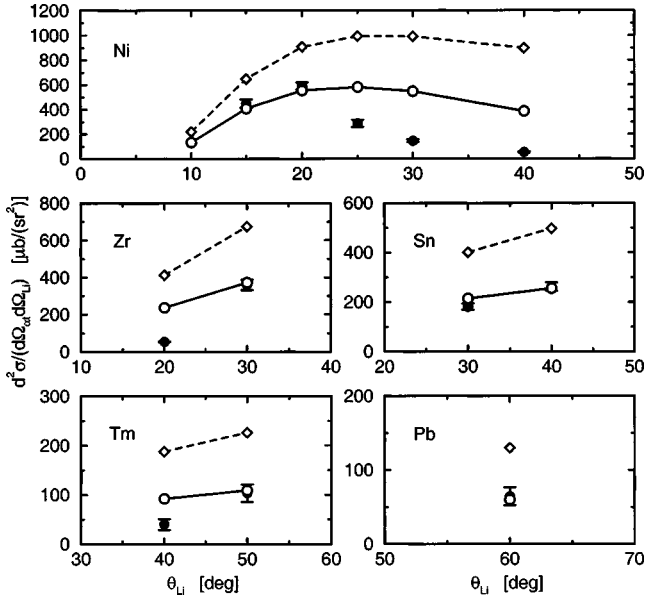

FIG. 21. Double differential cross section for the excitation of the $7/2^-$ resonance in ^{7}Li for different targets and scattering angles. Solid circles: experimental data, diamonds: first order calculation with $E1$ and $E2$ contributions, open circles: dynamical calculation.

$$\frac{d^3\sigma}{dE_{\alpha t}d\Omega_{\alpha t}d\Omega_{\rm Li}}=\frac{d\sigma_R}{d\Omega_{\rm Li}}\frac{1}{2J_i+1}\sum_{if}|a_{fi}(\vec{p}_{\alpha t})|^2\varrho_f \quad (19)$$

for the breakup in the semiclassical approximation. The sum runs over all values M_i of the initial state and all final states of a given final momentum $\vec{p}_{\alpha t}$. The density of final states is denoted by ϱ_f and $d\sigma_R/d\Omega_{\rm Li}$ is the Rutherford cross section for the elastic ^{7}Li-target scattering.

VI. ANGULAR AND ENERGY DISTRIBUTIONS

A. Resonant breakup

In Fig. 21 experimental cross sections in the $v_\alpha \geqslant v_t$ branch for the breakup of ^{7}Li through the $\frac{7}{2}^-$ state at 2.16 MeV are shown in comparison with theoretical calculations for five different targets. The theoretical results were obtained by integrating the triple differential cross section over the energy range $2.06-2.26$ MeV. This sharp resonance is populated in first order via an $E2$ transition from the p-wave ground state. Because of its long lifetime (≈ 2100 fm/c) one would expect only small higher order corrections to the breakup cross section. However, the first order perturbation results considerably overestimate the cross section, while the dynamical calculation reasonably well reproduces the experimental data. Of course, the strength of the $E2$ transition, which is not known from other experiments, strongly depends on the nuclear model for the ^{7}Li system. Thus, a reduction of the $E2$ coupling from a modification of our simple potential model would result in a reduction of the first order cross section with better agreement with the experimental data. But we do not expect that reasonable change of the model would lead to the necessary reduction of the $E2$ coupling since the $E1$ transition in our model seems to be of

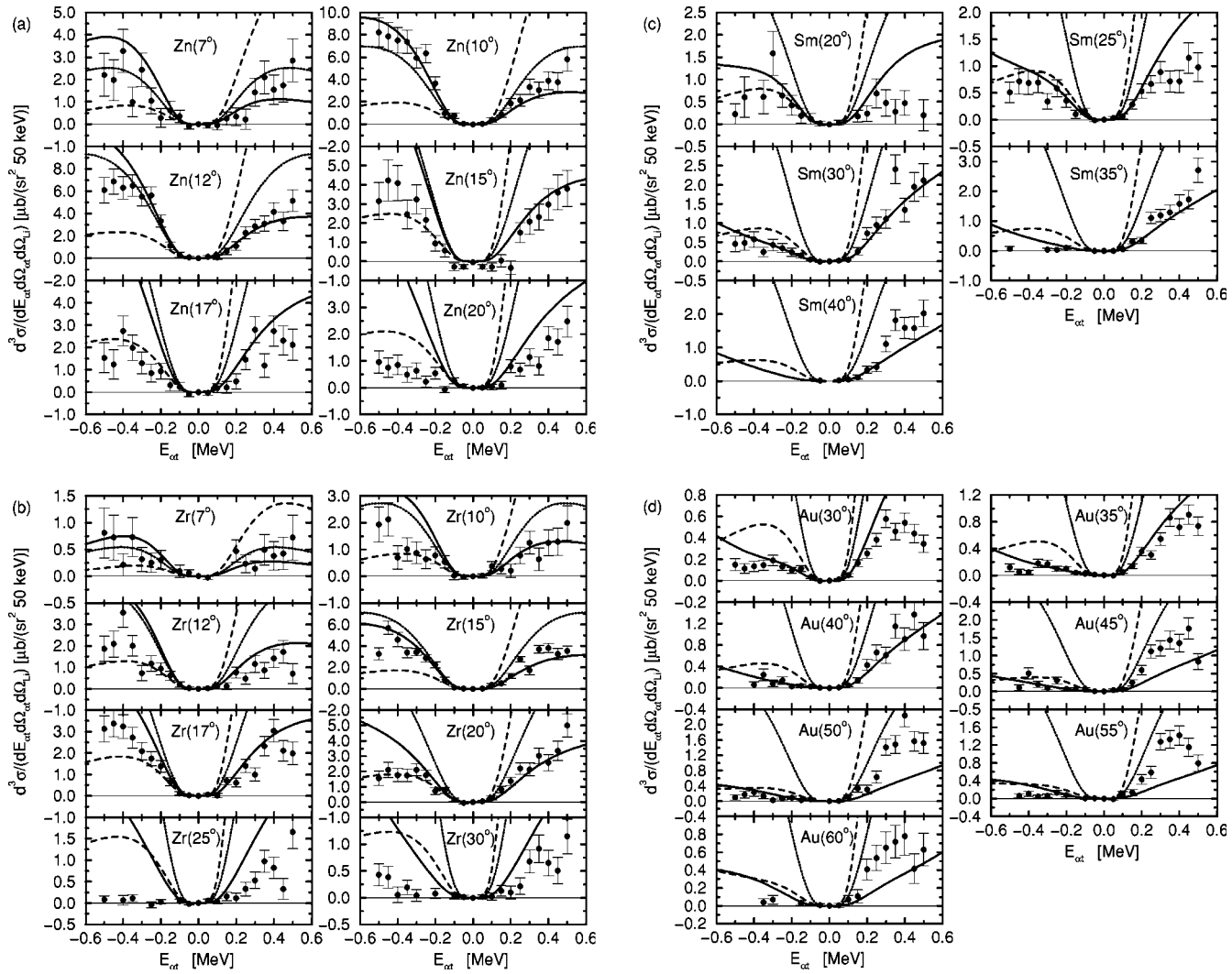

FIG. 22. (a) Triple differential cross section for the breakup of 42 MeV ^{7}Li on a ^{64}Zn target for different scattering angles as a function of the α-t energy. Positive (negative) energies correspond to the branch $v_\alpha \geqslant v_t$ ($v_\alpha \leqslant v_t$). Solid circles: experimental data, dotted line: first order $E1$ calculation, dashed line: first order $E1+E2$ calculation, solid line: dynamical calculation. (b) Same as (a), but for a ^{90}Zr target. (c) Same as (a), but for a ^{144}Sm target. (d) Same as (a), but for a ^{197}Au target.

correct size. In case of the ^{58}Ni target, the experimental cross section becomes much smaller as compared to the theoretical results at large scattering angles (larger than the grazing angle; see Table II). This can be related to nuclear breakup and absorption which can substantially modify the cross section for small impact parameters where projectile and target nucleus come very close to each other. In the case of the ^{90}Zr and ^{169}Tm target the results of the dynamical calculation still overestimate the experimental cross section which is not yet understood. Despite the model dependence of the interpretation, we conclude that higher order effects cannot be neglected in the Coulomb excitation to the *f*-wave resonant state.

B. Nonresonant breakup

Figure 22 shows triple differential cross sections $d^3\sigma/(dE_{\alpha t}d\Omega_{\alpha t}d\Omega_{\mathrm{Li}})$ as a function of relative energy for four targets and various scattering angles in comparison with theoretical calculations. Positive (negative) energies correspond to the case $v_\alpha \geqslant v_t$ ($v_\alpha \leqslant v_t$). This highly differential cross section is very sensitive to both interference effects from different partial waves and higher order effects. Strong forward-backward asymmetries can be observed in the energy dependence of the experimental data. A pure $E1$ first order calculation shows no asymmetry since at small relative energies only the *s*-wave state in the continuum is populated resulting in an isotropic emission of the fragments in the projectile system. At the same time, the cross section is becoming much too large at higher relative energies. A first order calculation including $E1$ and $E2$ transitions as well as the full dynamical calculation results in rather different energy dependence in both branches. Higher order effects are clearly seen in cross sections with $v_\alpha \geqslant v_t$ that are strongly reduced from the first order excitation with $E1$ and $E2$ multipoles. Note also that the same effects rather enhance cross sections with $v_\alpha \leqslant v_t$ for medium-Z targets (^{90}Zr and ^{64}Zn)

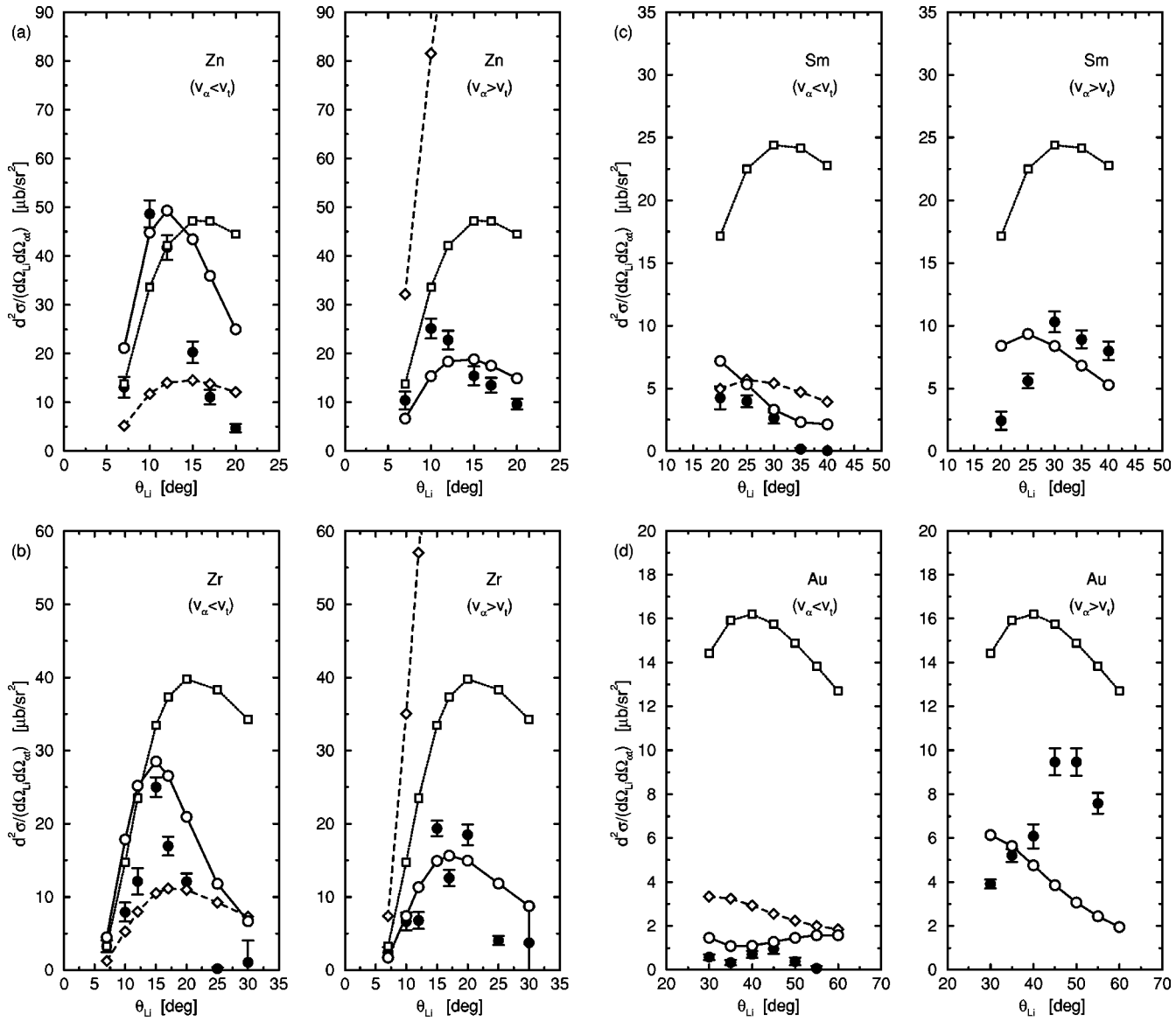

FIG. 23. (a) Double differential cross section for the breakup of 42 MeV ^{7}Li on a ^{64}Zn target as a function of the scattering angle for the two branches $v_\alpha \geqslant v_t$ (right) and $v_\alpha \leqslant v_t$ (left, see text). Solid circles: experimental data, squares: first order $E1$ calculation, diamonds: first order $E1+E2$ calculation, open circles: dynamical calculation. (b) Same as (a), but for a ^{90}Zr target. (c) Same as (a), but for a ^{144}Sm target. (d) Same as (a), but for a ^{197}Au target.

except at backward angles. Admixture of $E2$ multipole is typically seen in cross sections with $v_\alpha \leqslant v_t$ for ^{197}Au and ^{144}Sm, where both the first order and the dynamical calculations with $E1$ and $E2$ multipoles give similar cross sections that are consistent with the experimental data, whereas the first order Coulomb excitation with $E1$ multipole overestimate the data. Although there is no perfect reproduction of the experimental data, the results of the full dynamical calculation seem to be in better agreement with the experiment than the first order calculation.

Integrating the triple differential cross section for both branches over relative energy we obtain the corresponding the double differential cross sections

$$\frac{d^2\sigma}{d\Omega_{\alpha t} d\Omega_{\mathrm{Li}}} = \int_0^{0.5\ \mathrm{MeV}} dE_{\alpha t} \frac{d^3\sigma}{dE_{\alpha t} d\Omega_{\alpha t} d\Omega_{\mathrm{Li}}} \qquad (20)$$

as a function of the scattering angle. The results are shown in Fig. 23. It is obvious that the first order $E1$ calculation cannot explain the experimental data. Including the $E2$ contribution leads to a too strong forward-backward asymmetry. Only the full dynamical calculation shows a reasonable agreement with the experimental data, for both the asymmetry and the absolute cross section. As seen in the triple differential cross sections for medium-Z (^{64}Zn and ^{90}Zr) targets, higher order effects reduce the absolute cross section in the $v_\alpha \geqslant v_t$ branch, while they rather enhance that in the $v_\alpha \leqslant v_t$ branch except at backward angles where nuclear breakup may contribute. The three results of the first order $E1$, the first order $E1+E2$, and the dynamical calculations tend to merge at small angles for the medium-Z targets. This can be explained by the reduction of higher order effects and $E2$ multipole with decreasing scattering angle. Hence, the

$v_\alpha \geqslant v_t$ branch for small scattering angles and medium-Z targets is affected least of all by higher order effects and $E2$ multipole.

We remark that the semiclassical consideration of the postacceleration in Coulomb breakup (Sec. IV) is consistent with the present quantum-mechanical analysis of higher order effects. Both have revealed the importance of multistep Coulomb interactions between fragments (α,t) and the target, but in two different facets. The former emphasized the distortion of α-t relative kinetic energies, while the latter revealed the reduction and enhancement of cross sections.

It is now interesting to consider the difference between Coulomb postacceleration after breakup and channel-coupling before breakup. It should be noted that the terminology ''post-Coulomb acceleration'' is used throughout the present paper in a broader sense, including these two effects. The semiclassical consideration took a geometrical view of breakup. It was assumed that Coulomb excitation to a continuum state takes place at the distance of closest approach. After the excitation the projectile ^{7}Li continued to move along a hyperbolic trajectory until the tunneling through the Coulomb barrier is completed. After the tunneling, the ^{7}Li lost its identity of a nucleus by liberating constituent clusters (α and t), that are independently accelerated in the target Coulomb field without interacting each other. Therefore, this is purely Coulomb postacceleration after breakup. When $E_{\alpha t}$ is small, the Coulomb postacceleration is strongly suppressed because of the large tunneling lifetime. Note that possible coupled-channel effects before the breakup by tunneling are beyond the semiclassical discussion.

In contrast, in the quantum-mechanical treatment, the development of the ^{7}Li wave function under the time-dependent Coulomb perturbation was investigated by solving a Schrödinger equation. Similarly, the center of mass of the ^{7}Li was assumed to move on a hyperbolic trajectory. During the c.m. motion along the classical trajectory, the Coulomb perturbation modifies α-t relative motion significantly, where the channel coupling before breakup and the Coulomb postacceleration after breakup are treated on the same footing. Although there is no strict separation, one way of separating these two effects would be to calculate the expectation value of the α-t distance in the quantum-mechanical calculation. If one simply calculates the expectation value as a function of time one will find always a value which is very small since most of the total wave function is in the ^{7}Li ground state. Only a small fraction is in an excited state. Therefore, one has to project out the ground state part of total wave function (see Sec. V B). As long as the expectation value would be smaller than the channel radius of ^{7}Li, it could be the coupled-channel effect caused by multistep Coulomb excitation. Although the study of these two effects in the quantum-mechanical calculation is worthwhile, we leave a detailed investigation in the future.

C. Forward-backward ratio

In Fig. 24 the forward-backward ratio

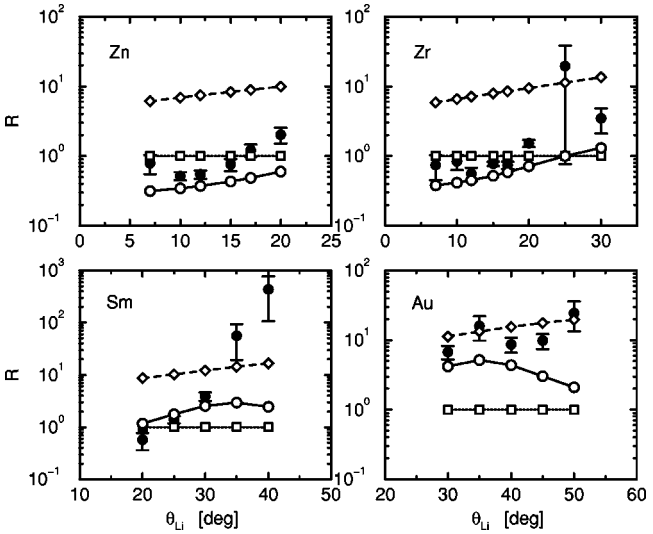

FIG. 24. Forward-backward ratio R of energy integrated cross sections for the breakup of 42 MeV ^{7}Li as a function of the scattering angle for different targets (see text). Solid circles: experimental data, squares: first order $E1$ calculation, diamonds: first order $E1+E2$ calculation, open circles: dynamical calculation.

$$R=\frac{d^2\sigma}{d\Omega_{\alpha t}d\Omega_{\mathrm{Li}}}(v_\alpha \geqslant v_t) \Big/ \frac{d^2\sigma}{d\Omega_{\alpha t}d\Omega_{\mathrm{Li}}}(v_\alpha \leqslant v_t) \quad (21)$$

of the energy integrated cross sections is shown for four different targets as a function of the scattering angle. Again, we observe a too strong asymmetry from the first order $E1+E2$ calculation, whereas the first order $E1$ calculation shows no asymmetry at all. The dynamical calculation can reasonably explain the observed asymmetry although there remain some differences at larger scattering angles which may be related to nuclear effects.

We cannot expect a complete agreement of the calculation to the experiment within our simple model of ^{7}Li, though it, in principle, can be improved. In addition to this, nuclear contributions to the breakup need to be investigated thoroughly. However, it is beyond the scope of the present analysis. Also, such effects as interference from different classical trajectories as well as a change of the classical trajectory due to the overlap of projectile and target are beyond the semiclassical treatment employed here.

VII. ASTROPHYSICAL *S* FACTOR

The potential model of ^{7}Li employed in this work predicted astrophysical S factors for $t(\alpha,\gamma)^7$Li as shown by the solid line in Fig. 1. These S factors lie somewhere between the upper limit set by Refs. [6,9] and the lower limit by Ref. [5] at small energies. The energy dependence rather follow the result of Ref. [8] though absolute values are slightly different. With these S factors, the experimental data were reasonably reproduced by the dynamical calculation of Coulomb breakup with two key ingredients: higher order effects and mixture of $E1$ and $E2$ multipoles.

The method of Coulomb breakup [1] goes in the other way around, aiming at deducing S factors from the data

rather than reproducing the data with S factors. The method was applied for the first time to $t(\alpha,\gamma)^7$Li [9]. The data of ^{7}Li breakup at 63 and 42 MeV nearly exhibited a *universal* energy dependence of the reduced transition probability. Based on the empirical parallelism in nuclear and Coulomb excitation, the energy dependence of the astrophysical S factor for $t(\alpha,\gamma)^7$Li was deduced in the energy range 80–980 keV. After being normalized to $S(0.5\ \mathrm{MeV})=0.06$ keV b, the S factors resulted in a strong energy dependence below 300 keV.

In this first Coulomb breakup experiment, cross sections were measured in the collinear branch of $v_\alpha \leqslant v_t$. The present semiclassical consideration has, however, shown that α-t relative kinetic energies at the time of breakup are readily modified by the post-Coulomb acceleration when observed asymptotically. As a result, it destroys correct energy dependence of S factors.

Instead, cross sections in the $v_\alpha \geqslant v_t$ branch can be used provided that they are dominated by one-step Coulomb excitation with $E1$ multipolarity. In this respect, the present quantum-mechanical analysis (Sec. VII) has shown that higher order effects and $E2$ multipole tend to diminish for medium-Z targets at very forward angles. Cross sections rapidly decrease at these angles because the breakup becomes adiabatic, where the adiabaticity parameter

$$\xi(\theta)=\frac{E_\gamma a}{\hbar v}\frac{1}{2}\left(1+\frac{1}{\sin\frac{\theta}{2}}\right) \tag{22}$$

becomes large. For a given transition from an initial state i to a final state f the strength of the excitation process and the importance of higher order effects are not independent. The strength parameter

$$\chi_{i\to f}^{E1}=\frac{Z_T e\langle f|M(E1)|i\rangle}{\hbar v b} \tag{23}$$

is a measure for the coupling strength between two states during the excitation [41]. For large χ we expect strong higher order effects. Figure 25 shows the strength parameter and the adiabaticity parameter for ^{197}Au and ^{90}Zr. We find that cross sections decrease at small angles because the breakup becomes adiabatic and ξ increases. At the same time the strength parameter χ decreases, which represents smaller higher order effects. A small target charge reduces higher order effects, too.

We attempted to deduce astrophysical S factors with the data for ^{90}Zr and ^{64}Zn at 7°–15°. Double differential cross sections for Coulomb excitation with $E1$ multipole are expressed by

$$\frac{d^2\sigma_{E1}}{d\Omega dE_\gamma}=\frac{9}{16\pi^3}\frac{Z_T^2\alpha}{E_\gamma}\left(\frac{v}{c}\right)^2\frac{df_{E1}(\xi,\theta)}{d\Omega}\sigma_{E1}^{\mathrm{photo}}, \tag{24}$$

with photoabsorption cross section $\sigma_{E1}^{\mathrm{photo}}$. Here α is the fine structure constant and E_γ is photon energy. The first-order perturbation theory of Coulomb excitation was used to calculate $df_{E1}(\xi,\theta)/d\Omega$ with the symmetrized adiabaticity parameter [26]. The photoabsorption cross section is related to the radiative capture cross section $\sigma_{E1}^{\mathrm{capt}}$ by detailed balance theorem:

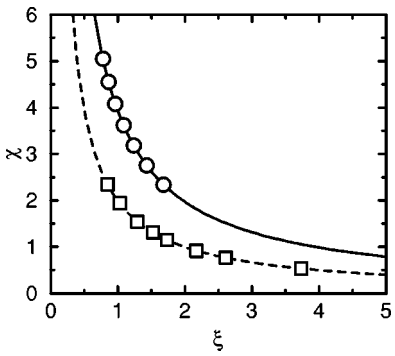

FIG. 25. Schematic relation of the strength parameter χ and the adiabaticity parameter ξ for the present experiment with ^{197}Au (solid line) and ^{90}Zn (dashed line) targets. Circles and squares correspond to a transition from the ^{7}Li ground state to the α-t breakup threshold at the experimental scattering angles (see Table I) for ^{197}Au and ^{90}Zn targets, respectively.

$$\sigma_{E1}^{\mathrm{capt}}=\frac{2(2j_a+1)}{(2j_b+1)(2j_c+1)}\frac{k_\gamma^2}{k^2}\sigma_{E1}^{\mathrm{photo}}, \tag{25}$$

where j is the particle spin ($a\equiv{}^7$Li, $b\equiv\alpha$, $c\equiv t$), k is the wave number in the $\alpha+t$ channel, and k_γ is the photon wave number. The astrophysical S factor $S(E_{\alpha t})$ is defined by

$$\sigma_{E1}^{\mathrm{capt}}(E_{\alpha t})=\frac{1}{E_{\alpha t}}S(E_{\alpha t})\exp(-2\pi\eta). \tag{26}$$

Since the Coulomb breakup experiment gives $S(E_{\alpha t})$ for the ground state transition, the branching ratio $\gamma_1/\gamma_0=0.453$ was assumed [8]. The $S(E_{\alpha t})$ thus deduced for ^{64}Zn and ^{90}Zr are shown in Figs. 26(a) and 26(b), respectively. Due to the adiabatic trend of the breakup cross section, statistical uncertainties are quite large; data at these angles fluctuate to within 1σ uncertainties in most cases. Weighted average was taken for the ^{64}Zn and ^{90}Zr data sets separately. Results are shown by the solid circles in the figures. Finally the two data sets were combined. As shown in Fig. 26(c) the resultant $S(E_{\alpha t})$ show a very moderate energy dependence. The S factors tend to be smaller than those of the direct measurements. Possibly there are still higher order effects in the data which tend to reduce the cross section in the $v_\alpha \geqslant v_t$ branch. It should be pointed out that if cross sections in the $v_\alpha \leqslant v_t$ branch are used, the result of the previous Texas A&M experiment is reproduced (open and solid triangles). However, these are most likely Coulomb distorted and should be replaced by the present $S(E_{\alpha t})$.

VIII. CONCLUSIONS

Breakup of ^{7}Li through continuum states immediately above the α-t threshold (2.47 MeV) and the $7/2^-$ state was

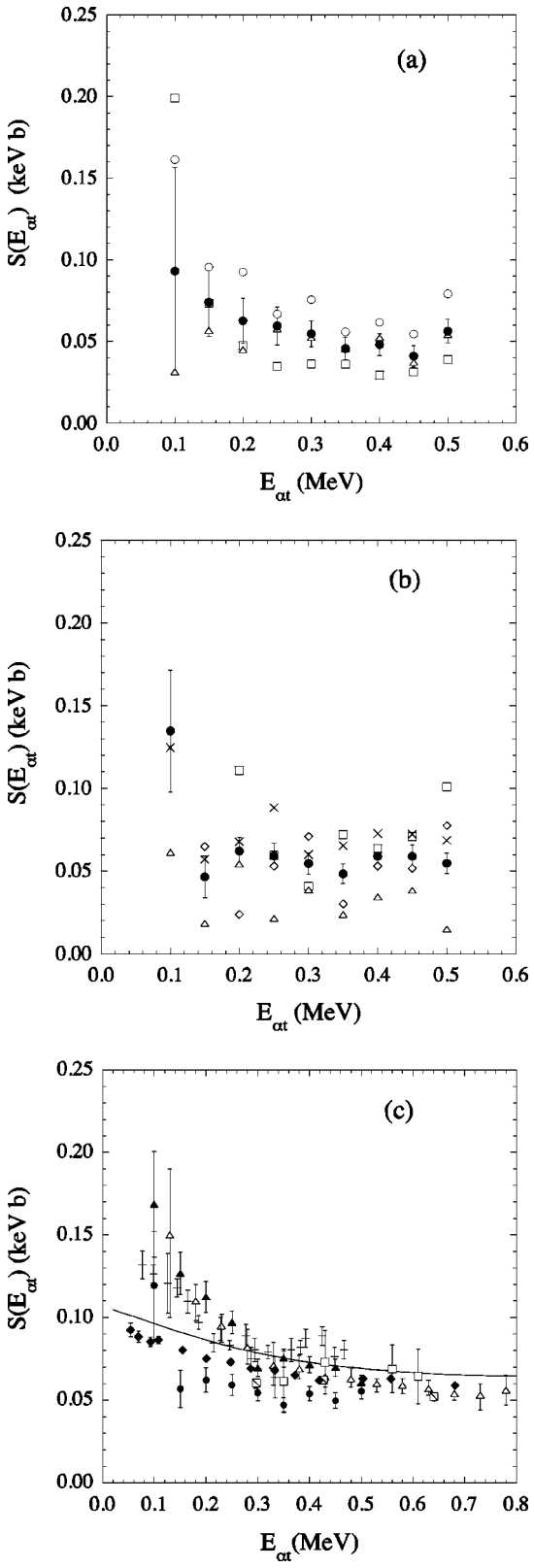

FIG. 26. Astrophysical S factors deduced from the ^{64}Zn data set (a) and the ^{90}Zr data set (b) (open squares: 7°, open diamonds: 10°, open triangles: 12°, crosses: 15°); Weighted-average values of S factors obtained by combining the two data sets (c). (Solid circles: $v_\alpha \geqslant v_t$, solid triangles: $v_\alpha \leqslant v_t$.) For comparison, currently available S factors are also shown with the same keys as in Fig. 1.

experimentally investigated to deduce information on radiative capture process $t(\alpha,\gamma)^7$Li in conjunction with big-bang nucleosynthesis. Coincidence measurements of breakup fragments, α and t, were performed in the collinear detection geometry with the broad range magnetic spectrograph.

The close examination of energy spectra of coincident α particles and tritons has revealed that the breakup kinematics at $E_{\alpha t}=0$ follow asymptotic breakup reaction, independent of target and detection angle. In an analogy to the α-decay theory, the tunneling lifetime of continuum states in ^{7}Li that are bound by a Coulomb barrier between α and t was evaluated. The transmission probability was calculated in the WKB approximation. It was found that the lifetime is significantly larger than the nuclear transit time. It can become larger than that of the $7/2^-$ state at 4.63 MeV ($\Gamma=93\pm8$ keV; $\tau\approx2100$ fm/c) at small energies. Thus, it was concluded that the nonresonant breakup of astrophysical relevance is not prompt but delayed breakup. As a result, the Coulomb postacceleration after breakup is strongly suppressed by the quantum tunneling.

Using the tunneling lifetimes, we semiclassically evaluated the effect of the postacceleration on $E_{\alpha t}$ assuming that the Coulomb excitation takes place at the distance of closest approach in the Rutherford trajectory. The assumption was reasonably supported by the first-order perturbation calculation of Coulomb excitation. It was found that $E_{\alpha t}$ in the collinear branch of $v_\alpha \geqslant v_t$ are essentially unaltered by the postacceleration on their way to the asymptotic region, while these in the $v_\alpha \leqslant v_t$ branch is severely Coulomb distorted.

The dynamical calculations of Coulomb excitation were performed by solving the time-dependent Schrödinger equation. A simple potential model of ^{7}Li was employed. The dynamical calculations reasonably reproduced cross sections of both resonant and nonresonant breakup, indicating the importance of higher order effects and mixture of $E1$ and $E2$ multipoles. The higher order effects strongly reduce breakup cross sections in the $v_\alpha \geqslant v_t$ collinear configuration. In the $v_\alpha \leqslant v_t$ branch, the same effects rather enhance nonresonant cross sections for medium Z targets except at backward angles. Admixture of the $E2$ multipole was typically seen as the reduction of the $v_\alpha \leqslant v_t$ cross sections for heavy targets.

Considering the dominance of the first-order $E1$ nature in adiabatic Coulomb breakup, the small angle data for medium-Z targets in the $v_\alpha \geqslant v_t$ branch were used to deduce astrophysical S factors for $t(\alpha,\gamma)^7$Li. The resultant S factors $S(E_{\alpha t})$ were less energy dependent than those from the previous Coulomb breakup experiment at Texas A&M. The previous $S(E_{\alpha t})$ based on cross sections in the $v_\alpha \leqslant v_t$ branch are most likely Coulomb distorted and revised in the present work.

ACKNOWLEDGMENTS

We would like to thank the accelerator crew of the Tandem Accelerator Center (University of Tsukuba) headed by Professor K. Furuno for providing high-quality and intense beams of ^{7}Li and the technical staff for strong support to the experimental equipment and the data acquisition. This work was supported by the Japan Ministry of Education, Science,

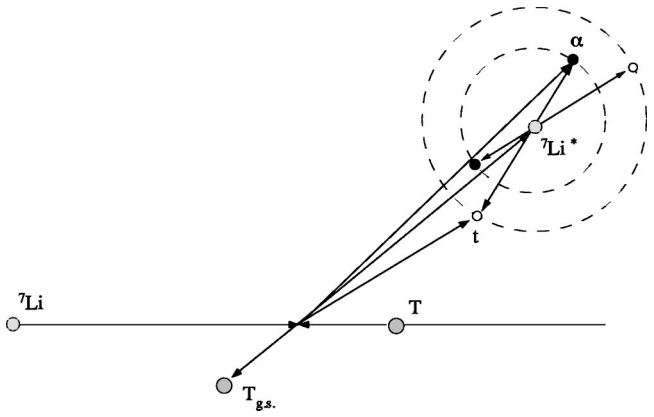

FIG. 27. Velocity diagram of breakup of projectile a into two fragments b and c in the target field.

Sports and Culture, the Japan Private School Promotion Foundation, and the U.S. Department of Energy under Grant No. DE-FG03-93ER40773.

APPENDIX: KINEMATICS OF PROJECTILE BREAKUP

Here we present some useful kinematical formulas associated with the post-Coulomb acceleration in projectile breakup reactions. Let us consider breakup of a projectile at a distance r from a target nucleus in the c.m. system. The projectile breakup is divided into two stages: excitation of the projectile (a) to a particle-unbound state ($a+T\rightarrow a^*+T$) and decay of the state into a reaction channel consisting of two charged particles ($a^*\rightarrow b+c$). The particle-unbound state can be either a resonant state or a nonresonant (continuum) state. The velocity diagram of the two stages is shown in Fig. 27.

In the stage of inelastic excitation, kinetic energies of the projectile at the distance r is given by

$$E_a(r)=\frac{A_T}{A_a+A_T}\left(E_0-E_x-\frac{Z_aZ_Te^2}{r}\right), \tag{A1}$$

where A_a and A_T (Z_a and Z_T) are the mass (charge) numbers of the projectile and target, respectively, E_0 is the bombarding energy, and E_x is the excitation energy. For simplicity, we use the mass number instead of mass except for calculating reaction Q values. In the decay stage, kinetic energies of breakup fragments (b, c) at the distance r are given [1] by

$$E_b^l(r)=\frac{A_b}{A_a}E_a(r)+\frac{\mu}{A_b}E_{bc}\mp 2\sqrt{\frac{\mu}{A_a}E_aE_{bc}}\cos\Phi \tag{A2}$$

and

$$E_c^l(r)=\frac{A_c}{A_a}E_a(r)+\frac{\mu}{A_c}E_{bc}\mp 2\sqrt{\frac{\mu}{A_a}E_aE_{bc}}\cos\Phi, \tag{A3}$$

where $A_{b(c)}$ is the fragment mass number and in the definition of the reduced mass μ_{bc} one has, e.g., $\mu_{bc}=A_bA_c/(A_b+A_c)$. The superscript l stands for a local kinetic energy defined at the distance r. E_{bc} is a relative kinetic energy given by $E_{bc}=E_x-S$ where the separation energy is defined by $S=[m_b+m_c-m_a]c^2$ with masses m_i. In the collinear breakup, $\Phi=0$.

The breakup fragments (b and c) are accelerated in the Coulomb field of a target nucleus by

$$\frac{A_T}{A_a+A_T}\frac{Z_iZ_Te^2}{r}, \tag{A4}$$

where $i=b$ or c.

Therefore, their final energies are

$$E_i(r)=E_i^l(r)+\frac{A_T}{A_a+A_T}\frac{Z_iZ_Te^2}{r}. \tag{A5}$$

In the breakup at $E_{bc}=0$,

$$E_i(r)=\frac{A_i}{A_a}\frac{A_T}{A_a+A_T}(E_0-E_x)+\frac{A_T}{A_a+A_T}\frac{Z_i^{\rm eff}Z_Te^2}{r} \tag{A6}$$

with the effective charge number

$$Z_i^{\rm eff}=A_i\left(\frac{Z_i}{A_i}-\frac{Z_a}{A_a}\right). \tag{A7}$$

In the asymptotic breakup (breakup at the distance of *infinity* compared to the size of a nucleus) at $E_{bc}=0$, the fragment energy is given by

$$E_i(\infty)=\frac{A_i}{A_a}\frac{A_T}{A_a+A_T}(E_0-E_x). \tag{A8}$$

From Eqs. (A6) and (A8), the relation between breakup at r and asymptotic breakup is given by

$$E_i(r)=E_i(\infty)+\Delta_i \tag{A9}$$

with

$$\Delta_i=\frac{A_T}{A_a+A_T}\frac{Z_i^{\rm eff}Z_Te^2}{r}. \tag{A10}$$

In the case where $Z_a/A_a=Z_b/A_b=Z_c/A_c$, there arises no Coulomb shift:

$$E_i(r)=E_i(\infty). \tag{A11}$$

[1] G. Baur, C. A. Bertulani, and H. Rebel, Nucl. Phys. **A458**, 188 (1986).
[2] G. Baur and H. Rebel, J. Phys. G **20**, 1 (1994).
[3] G. Baur and H. Rebel, Annu. Rev. Nucl. Part. Sci. **46**, 321 (1996).
[4] M. S. Smith and L. H. Kawano, Astrophys. J., Suppl. Ser. **85**, 219 (1993).
[5] G. M. Griffiths *et al.*, Can. J. Phys. **39**, 1397 (1961).
[6] U. Schröder *et al.*, Phys. Lett. B **192**, 55 (1987).
[7] S. Burzyński, K. Czerski, A. Marcinkowski, and P. Zupranski,

Nucl. Phys. **A473**, 179 (1987).
[8] C. R. Brune, R. W. Kavanagh, and C. Rolfs, Phys. Rev. C **50**, 2205 (1994).
[9] H. Utsunomiya *et al.*, Phys. Lett. B **211**, 24 (1988); Nucl. Phys. **A511**, 379 (1990); Phys. Rev. Lett. **65**, 847 (1990); **69**, 863(E) (1992).
[10] J. Hesselbarth *et al.*, Z. Phys. A **331**, 365 (1988); Phys. Rev. Lett. **67**, 2773 (1991).
[11] H. Jelitto *et al.*, Z. Phys. A **332**, 317 (1989).
[12] J. Kiener *et al.*, Z. Phys. A **332**, 359 (1989); **339**, 489 (1991); Phys. Rev. C **44**, 2195 (1991); Nucl. Phys. **A552**, 66 (1993).
[13] A. C. Shotter *et al.*, Phys. Rev. Lett. **46**, 12 (1981); Phys. Lett. **53A**, 1539 (1984); J. Phys. G **14**, L169 (1988).
[14] J. Yorkston *et al.*, Nucl. Phys. **A524**, 495 (1991).
[15] S. B. Gazes *et al.*, Phys. Rev. Lett. **68**, 150 (1992).
[16] J. E. Mason *et al.*, Phys. Rev. C **45**, 2870 (1992).
[17] H. Utsunomiya *et al.*, Phys. Lett. B **416**, 43 (1998).
[18] F. Ajzenberg-Selove, Nucl. Phys. **A490**, 1 (1988).
[19] L. C. Northcliffe and R. F. Schilling, Nucl. Data Tables **A7**, 233 (1970).
[20] Y. Tokimoto and H. Utsunomiya, Nucl. Instrum. Methods Phys. Res. A **434**, 449 (1999).
[21] D. D. Clayton, *Principles of Stellar Evolution and Nucleosynthesis* (The University of Chicago Press, Chicago, 1983).
[22] Claus E. Rolfs and Williams S. Rodney, *Cauldrons in the Cosmos* (The University of Chicago Press, Chicago, 1988).
[23] H. A. Bethe, Rev. Mod. Phys. **9**, 69 (1937).
[24] T. Kajino, Nucl. Phys. **A460**, 559 (1986), and references therein.
[25] G. Baur and M. Weber, Nucl. Phys. **A504**, 352 (1989).
[26] K. Alder, A. Bohr, T. Huus, B. Mottelson, and A. Winther, Rev. Mod. Phys. **28**, 432 (1956).
[27] P. Banerjee, I. J. Thompson, and J. A. Tostevin, Phys. Rev. C **58**, 1042 (1998).
[28] C. H. Dasso, S. M. Lenzi, and A. Vitturi, Nucl. Phys. **A639**, 635 (1998); Phys. Rev. C **59**, 539 (1999).
[29] S. Typel and G. Baur, Nucl. Phys. **A573**, 486 (1994).
[30] S. Typel and G. Baur, Phys. Rev. C **50**, 2104 (1994).
[31] S. Typel, H. H. Wolter, and G. Baur, Nucl. Phys. **A613**, 147 (1997).
[32] C. A. Bertulani and L. F. Canto, Nucl. Phys. **A539**, 163 (1992).
[33] L. F. Canto, R. Donangelo, A. Romanelli, and H. Schulz, Phys. Lett. B **318**, 415 (1993).
[34] G. F. Bertsch and C. A. Bertulani, Nucl. Phys. **A556**, 136 (1993); Phys. Rev. C **49**, 2839 (1994).
[35] T. Kido, K. Yabana, and Y. Suzuki, Phys. Rev. C **50**, R1276 (1994); **53**, 2296 (1996).
[36] H. Esbensen, G. F. Bertsch, and C. A. Bertulani, Nucl. Phys. **A581**, 107 (1995).
[37] C. A. Bertulani, Nucl. Phys. **A587**, 318 (1995).
[38] H. Esbensen and G. F. Bertsch, Nucl. Phys. **A600**, 37 (1996).
[39] V. S. Melezhik and D. Baye, Phys. Rev. C **59**, 3232 (1999).
[40] S. Typel and H. H. Wolter, Z. Naturforsch. A **54**, 63 (1999).
[41] S. Typel and G. Baur, Phys. Rev. C **49**, 379 (1994).